Article

Calibrating the EGS Flow Stimulation Process for Basement Rock

Peter Leary [1,*], Peter Malin [1], Tero Saarno [2] and Ilmo Kukkonen [3]

[1] Advanced Seismic Instrument Research; pcl@asirseismic.com
[2] St1 Deep Heat Oy; tero.saarno@st1.fi
[3] University of Helsinki; ilmo.kukkonen@helsinki.fi
* Correspondence: pcl@asirseismic.com;

Abstract: We use Matlab 3D finite element fluid flow/transport modelling to simulate localized wellbore temperature events of order 0.05-0.1°C logged in Fennoscandia basement rock at ~ 1.5km depths. The temperature events are approximated as steady-state heat transport due to fluid draining from the crust into the wellbore via naturally occurring fracture-connectivity structures. Flow simulation is based on the empirics of spatially-correlated fracture-connectivity fluid flow widely attested by well-log, well-core, and well-production data. Matching model wellbore-centric radial temperature profiles to a 2D analytic expression for steady-state radial heat transport with Peclet number $P_e \equiv r_0\underline{\phi}v_0/D$ (r_0 = wellbore radius, v_0 = Darcy velocity at r_0, $\underline{\phi}$ = ambient porosity, D = rock-water thermal diffusivity), gives P_e ~ 10-15 for fracture-connectivity flow intersecting the well, and P_e ~ 0 for ambient crust. Darcy flow for model P_e ~ 10 at radius ~ 10 meters from the wellbore gives permeability estimate κ ~ 0.02Darcy for flow driven by differential fluid pressure between least principal crustal stress pore pressure and hydrostatic wellbore pressure. Model temperature event flow permeability κ_m ~ 0.02Darcy is related to well-core ambient permeability $\underline{\kappa}$ ~ 1μDarcy by empirical poroperm relation $\kappa_m \sim \underline{\kappa}\exp(\alpha_m\underline{\phi})$ for $\underline{\phi}$ ~ 0.01 and α_m ~ 1000. Our modelling of wellbore temperature events calibrates the concept of reactivating fossilized fracture-connectivity flow for EGS permeability stimulation of basement rock.

Keywords: EGS; crustal permeability; finite element flow modelling; crustal wellbore temperatures; wellbore injection; well logs; well core

---

1. Introduction

Winning significant quantities of heat energy from the Earth's deep crystalline rock heat store requires a scientific and technical understanding of rock fluid flow properties that has yet to be established. The long-standing short-fall in accessing basement rock heat energy at drillable depths [1-4]. is due principally to uncertainty how to send fluid from an injector wellbore to a producer wellbore at a sufficient rate through a sufficiently large volume of low-porosity/low-permeability crustal rock to justify drilling costs.

We address the current wellbore-to-wellbore flow process uncertainty by focusing on local crustal flow phenomena signaled by isolated wellbore temperature log events at 1-2 km depths in

Peer-reviewed version available at *Energies* **2017**, *10*, 1979; doi:10.3390/en10121979

Fennoscandia basement granites. The observed wellbore temperature events of order 0.05-0.1°C can be plausibly attributed to heat advective fluid flow into a newly drilled wellbore via residual fracture-connectivity networks in otherwise effectively impermeable basement rock [5-6]. The observed Fennoscandia wellbore temperature events are paralleled by instances of electrical conductivity deviations plausibly due to chemical ion transport in the same or similar flow systems.

Our heat advection transport modelling does not associate wellbore temperature events with flow in crustal faults taken to be quasi-planar in-plane dislocation slip surfaces that act as fluid conduits characterized by 'cubic law' laminar flow [7-8]. Rather, as in [5-6] we broaden the class of crustal fracture-connectivity structures to include the pervasive spatially-correlated percolation pathways attested by three empirical features of crustal rock observed worldwide:

(I) Well-log spatial fluctuation power $S(k)$ that scales inversely with spatial frequency k, $S(k) \sim k^{\beta}$, $\beta \sim 1.2 \pm 0.1$, over five decades of scale length, ~1/km < k < ~1/cm, recorded at 1-9km crustal depths in a wide range of geological settings [9-13];

(II) Well-core spatial fluctuation sequence correlation between porosity ϕ and the logarithm of permeability, $\delta\phi \propto \delta\log(\kappa)$, recorded at numerous oil/gas field reservoirs and for selected metamorphic well core [5-6,14-17];

(III) Well-productivity lognormality due to spatially correlated porosity, $\kappa \propto \exp(\alpha\phi)$, with $20 < \alpha < 40$ in conventional reservoir rock having normally distributed porosity $0.1 < \phi < .3$, and $300 < \alpha < 700$ in metamorphic rock core having normally distributed porosity $\phi \sim .01$ [5-6,18-21].

The poroperm relation $\kappa(x,y,z) \propto \exp(\alpha\phi(x,y,z))$, for $\phi(x,y,z)$ a stochastic field of spatially-correlated porosity, reproduces crustal fluid-flow heterogeneity at Dm-Hm flow scales attested by reservoir well-core sequences and lognormal groundwater, hydrocarbon, and hydrogeothermal well production distributions [19-23]. The lognormal crustal poroperm phenomenology expressed through the poro-connectivity parameter α implies that relatively small increases in the parameter generate relatively high increases permeability without implicitly increasing porosity. Because of the multiplicative nature of permeability, doubling fracture-connectivity parameter α in a crustal volume can increase volume permeability by one to two orders of magnitude without having to do work against confining stresses to accommodate increased porosity. There is, therefore, an implicit energy argument that the crustal fluid-rock interaction processes that generate $\kappa(x,y,z) \propto \exp(\alpha\phi(x,y,z))$ flow heterogeneity do so as a consequence of a reduced crustal deformation energy budget.

Such fluid-rock interaction energetics may explain the persistence of rock-physical spectral scaling phenomenology $S(k) \sim 1/k$ to the 5-9km depth crusts recorded in the KTB scientific deep well [24]. In spite of decreasing porosity and permeability due to increased confining pressures at 5-10km depths, the $S(k) \sim 1/k$ spatial fluctuation scaling attested by reservoir flow systematics at 1-5km depths do not cease at greater depths. It can further be noted that the amplitudes of well-log spatial fluctuations do not diminish with extreme depth. It is thus logical to deduce fluid-rich

 doi:10.20944/preprints201709.0079.v1

Peer-reviewed version available at *Energies* **2017**, *10*, 1979; doi:10.3390/en10121979

poro-connectivity pathways and the associated spatial fluctuation complexity remains present in deep crustal rock as fossilized hydrated mineral infilling. KTB data discussed below illustrate the depth persistence of well-log fluctuation amplitudes and scaling relation (I). Further, KTB well-core data calibrate the (II)-(III) scaling parameter α at depth: as porosity decreases an order of magnitude with depth, $\phi \rightarrow 1\%$, the poro-connectivity scaling parameter increases by an order of magnitude, $\alpha \rightarrow 300$.

The Fennoscandia granite wellbore temperature events discussed here occur in rock of < ~1% porosity and < ~1μD permeability at confining pressures ~ 1-2km depth. Well-log fluctuation sequences in Fennoscandia basement rock preserve $S(k) \sim 1/k$ scaling. The observed naturally occurring 1.5km-deep wellbore temperature events are direct analogues for wellbore-centric fluid-rock interaction with *in situ* fracture-connectivity structures at Dm scales relevant to EGS wellbore-to-wellbore flow stimulation in basement rock.

2. Fennoscandia basement wellbore temperature events at 1.5km

Geothermal heat energy extracted from Fennoscandia basement rock can replace the current fossil-fuel demand made by the several hundred district heating plants supplying hot water to as many as a million homes throughout Finland. For Fennoscandia basement with geothermal gradient ~ 19^oC/km, supply of significant geothermal energy to district heating plants requires EGS couplets at depths ~ 5-7km. At a district heating plant in Espoo, immediately west of Helsinki, a 2km deep 100mm diameter pilot well, OTN1, was drilled, cored, and logged in advance of deeper drilling. Currently, two adjacent 305mm diameter wellbores, OTN2 and OTN3, now reach 3.3 and 5 km depths.

Pilot well OTN1 logs are observed to follow the power-spectral trend (I), and core poroperm properties for twenty core samples from depth intervals at 300 meters and 1300 meters follow poroperm spatial correlation (II). Well-core porosity is typically less than 1%, and permeability of order 1-10μD (10^{-18}-10^{-17}m^2). As discussed below, the empirical poroperm relation $\kappa(x,y,z) \propto \exp(\alpha\phi(x,y,z))$ valid for the measured value of $\alpha \sim 500$ for OTN1 is similar to values found for porosity-permeability data from the KTB well and the Borrowdale volcanics at the UK Sellafield nuclear facility. This discussion places OTN1 well-log spatial fluctuation and well-core poroperm data in a wider basement rock context provided by KTB, Fennoscandia and UK Nirex metamorphic basement rock data [24-28].

Peer-reviewed version available at Energies 2017, 10, 1979; doi:10.3390/en10121979

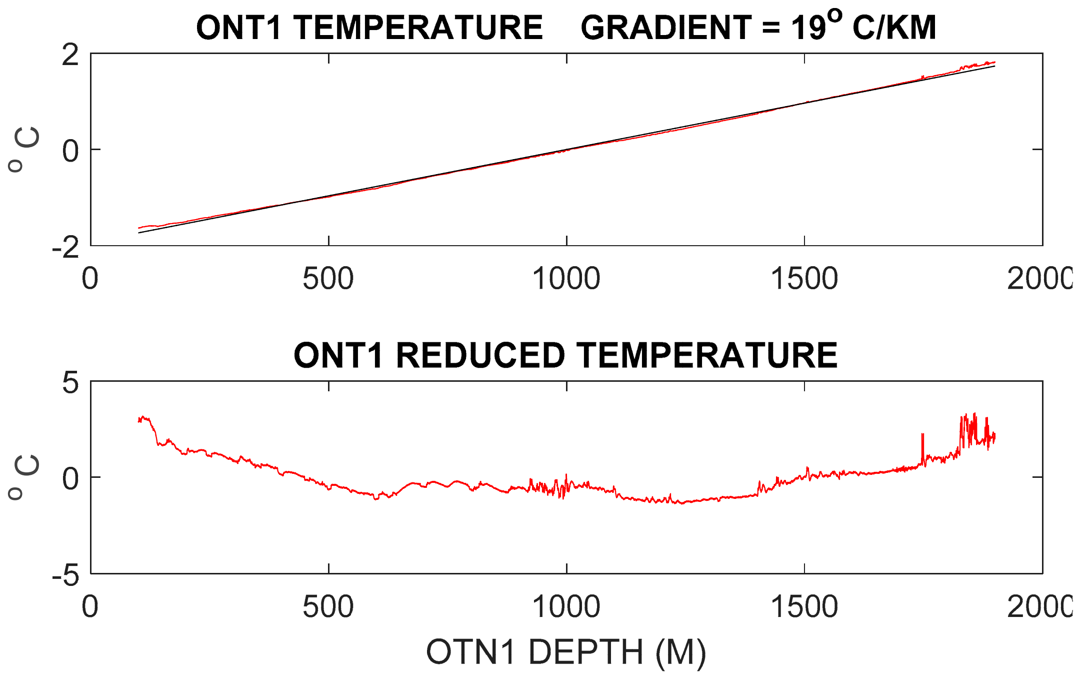

Figure 1. OTN1 temperatures (upper) and reduced temperatures (lower) between 100 and 1900 meters.

Figures 1-2 display the OTN1 pilot well temperature and reduced temperature profiles. The upper panel of Figure 1 shows a uniform gradient perturbed at the near-surface due to groundwater circulation, and at depth due to a section of unusually heterogeneous rock (with possible depth-related instrument effects). Removing the uniform temperature gradient, the lower Figure 1 panel highlights the effects of near-surface groundwater circulation to depth ~ 600 meters, and shows discrete wellbore intervals of considerable temperature fluctuation at 800-1100 meters and 1750-1850 meters. These intervals are associated with a complex, highly fractured and attenuative heterogeneous mafic gneissic rock. Our present interest lies in the more uniform granites between 1120 to 1700 meters, where the reduced temperature profile shows a series of sharp isolated positive temperature events.

Figure 2 expands the Figure 1 wellbore depth scale over the OTN1 1120-1700m granite interval, detailing the discrete 0.05-0.1°C temperature events of interest. A dozen or so 0.05-0.10°C positive temperature excursions of ~5-meter axial depth extent occur over a 600-meter span. The lower panel of Figure 2 displays the discrete temperature deviations relative to the upper-panel polynomial curve fit to the reduced temperature trace.

Preprints (www.preprints.org) | NOT PEER-REVIEWED | Posted: 18 September 2017 doi:10.20944/preprints201709.0079.v1

Peer-reviewed version available at Energies 2017, 10, 1979; doi:10.3390/en10121979

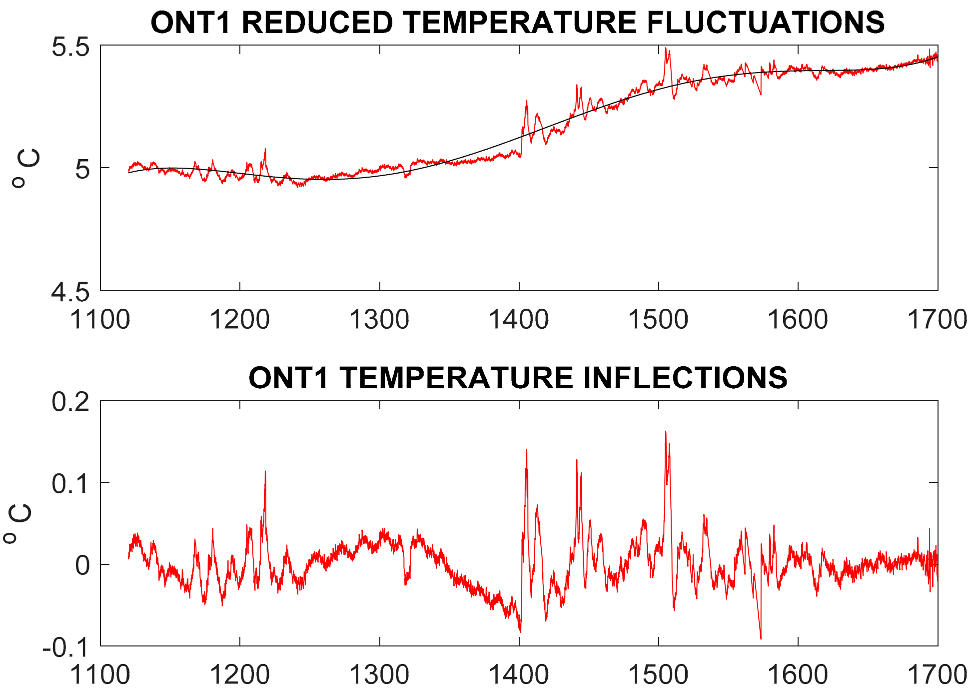

Figure 2. Reduced temperature log positive excursions (upper) and deviations from local temperature trending (lower) logged for the granitic rocks between 1120 and 1700 meters in the Espoo pilot well. The deviations can be plausibly associated with independent local fracture-connectivity flow structures that intersect the wellbore.

The Figure 2 OTN1 wellbore thermal fluctuations are unlikely to be caused by spatial variations in the thermal conductivity properties of rock. Spatial fluctuations of thermal conductivity for Fennoscandia basement rock measured over Hm intervals along a 2.5 km deep regional wellbore are restricted to 1% deviation from the mean [28]. Using the spectral character of the thermal conductivity data sequence to construct a representative 2D distribution of thermal conductivity spatial fluctuations, Figure 3 indicates that temperature fluctuations expected from thermal conductivity fluctuations are unlikely to exceed 0.005°C. The Figure 2 thermal deviations are 10 to 20 times the level attributable to spatial variations in thermal conductivity.

Preprints (www.preprints.org) | NOT PEER-REVIEWED | Posted: 18 September 2017 doi:10.20944/preprints201709.0079.v1

Peer-reviewed version available at Energies 2017, 10, 1979; doi:10.3390/en10121979

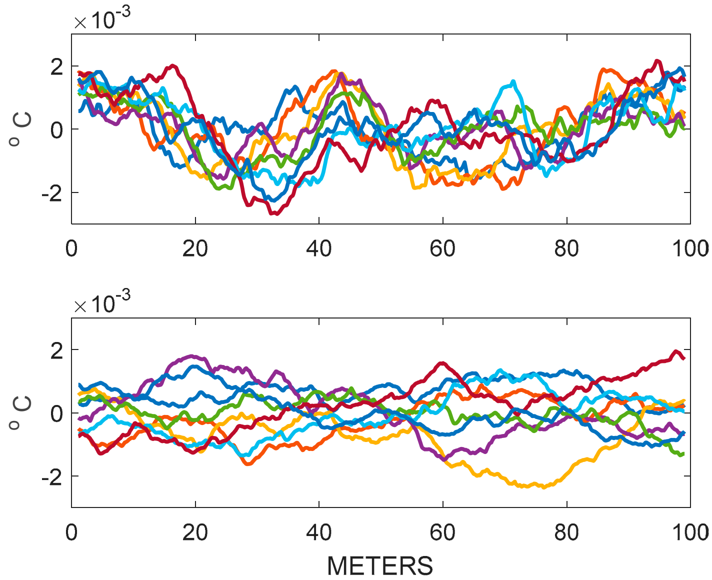

Figure 3. Representative temperature fluctuations for characteristic spatial variation in Fennoscandia basement rock thermal conductivity. Computation based on Hm scale thermal conductivity sequences from 2.5 km wellbore [28].

Our working hypothesis for the physical process leading to the Figure 2 OTN1 temperature events is that isolated fracture-connectivity structures in the crust intersect the wellbore and feed warmer crustal water into the cooler wellbore fluid column. We assume that the crustal fluid flow system is approaching a steady state in which the amplitude and spatial distribution of the temperature incursions change slowly.

Figure 4 illustrates steady-state fluid mechanical heat transport incursion using a 2D vertical planar pressure front moving fluid across a horizontal rock-fluid interface. Warm colors represent the hotter low-permeability crustal rock at higher fluid pressure, and cool colors represent the colder high-permeability wellbore fluid at lower fluid pressure. In the center of the Figure 4 crustal block, a narrow channel of higher crustal permeability intersects the wellbore to permit warmer crustal fluid at higher pressure to flow into the cooler wellbore fluid at lower pressure. The wellbore fluid temperature is elevated above its background level at the site where crustal waters enter the wellbore fluid; model side boundaries are set to zero-flow conditions. The resultant steady-state interface wellbore temperature profile is given in the lower panel. The lower panel also shows that away from the localized fracture-connectivity channel, fluid can leak from the crustal interior into the wellbore to generate small temperature fluctuations flanking the central temperature event. Such disseminated temperature fluctuations along the wellbore may be present in the Figure 2 wellbore temperature data.

Figure 4 also illustrates in 2D the global mesh nature of our 3D finite element computations discussed below. As access to deep crustal fluids is generally via a wellbore, slow or rapid percolation passage of wellbore fluid into or out of a surrounding crustal rock volume can be defined entirely by a stochastic permeability distribution within a global volumetric mesh. For

doi:10.20944/preprints201709.0079.v1

Peer-reviewed version available at *Energies* **2017**, *10*, 1979; doi:10.3390/en10121979

illustration purposes, the wellbore fluid is included in the flow simulation as a high-permeability flow component embedded in the global mesh across the rectangular model domain. Finite element computation simulates heat advection through the crustal-section flow-channel in parallel with heat conduction in the crust and the wellbore fluid. Inspection of Figure 4 shows that the spatially variable fluid flow geometry will give a variable value for the planar-flow Peclet number, $P_e \equiv v_0 \varrho C L/K$, where v_0 = fluid flow velocity, ϱC = volumetric heat capacity of water, L = layer thickness, and K = thermal conductivity of rock, across the crustal section [29]. The relation of Peclet number to fluid flow velocity links observed temperature distributions to crustal fluid flow structures.

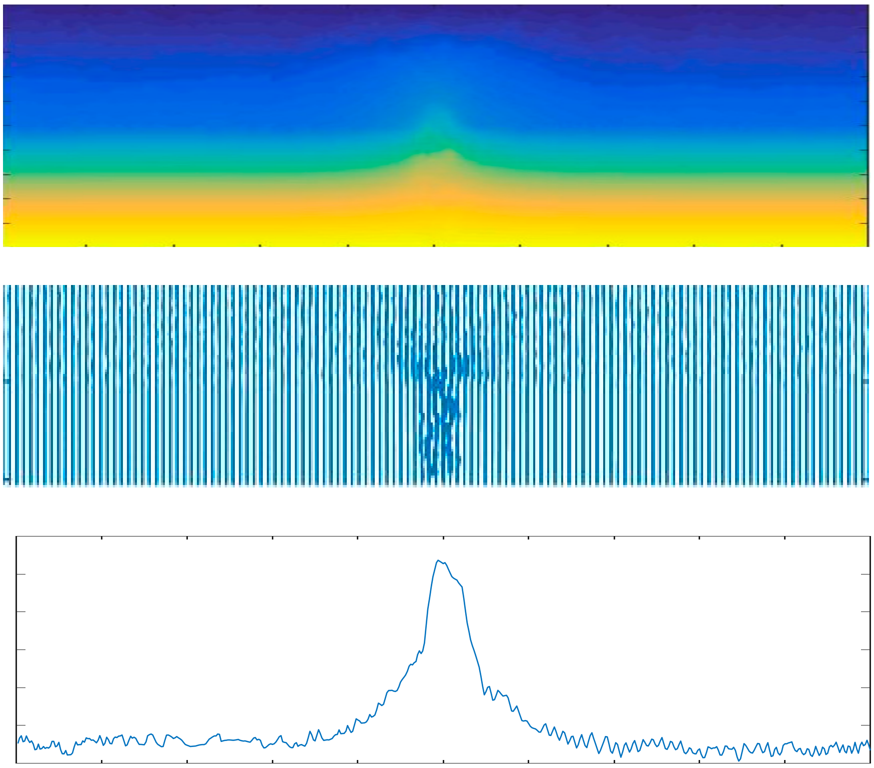

Figure 4. (Upper) Simulation of Figure 2 temperature events as heat transport from a hotter low-permeability medium (yellow-orange layer representing crustal rock) to a colder high-permeability medium (green-blue layer representing wellbore fluid). (Middle) Velocity vectors representing fluid flow in Figure 2 fracture-connectivity structure entering the wellbore; additional flow from the crust into the wellbore can be seen along the entire interface. (Lower) Temperature profile measured along the wellbore-crust interface in simulation of Figure 2 wellbore axial temperature profiles.

The Figure 4 2D mesh construction is for heat advection concept and computational mesh illustration purposes only. The following 3D wellbore-centric fluid flow computations treat the narrow-gauge wellbores as geometric flow boundaries outside the global mesh construction. As in Figure 4 for 2D flow, 3D model axial variation of wellbore-centric radial flow Peclet number computed for OTN1 temperature events converts observed wellbore axial temperature distributions into estimates of radial heat advective fluid flow for fracture-connectivity flow

Preprints (www.preprints.org) | NOT PEER-REVIEWED | Posted: 18 September 2017 doi:10.20944/preprints201709.0079.v1
Peer-reviewed version available at Energies 2017, 10, 1979; doi:10.3390/en10121979

structures. Axial temperature distributions along wellbore axial profiles thus become a diagnostic tool for investigating wellbore-centric fluid flow processes in crustal rock.

3. 3D global mesh finite element modelling of basement rock wellbore temperature events

Empirical crustal property (I) establishes the existence of spatially-correlated poroperm structures at all scales and at all drilling-accessed depths in the crust. In parallel, empirical crustal flow properties (II)-(III) establish the poro-connectivity flow mechanics at all scales for wellbore-accessed crustal volumes. On the strength of empirics (I)-(III), we interpret the Figure 2 set of wellbore-logged basement rock thermal event structures in terms of the 'canonical' or 'type' crust-to-wellbore or wellbore-to-crust fluid flow constructs sketched in Figure 4.

Given the broad evidentiary base for ambient crustal flow properties (I)-(III), it is logical to expect that when a wellbore intersects naturally-occurring flow structures, fluid at crustal confining pressures in the long-range spatially-correlated fracture-connectivity network flows into the hydrostatically under-pressured wellbore. If the intercepted flow structure is sufficiently large scale, heat will be advected into the wellbore by the inflowing fluid for a long enough period to be observed by wellbore logging. Comprehensive evidence for persistent Dm-scale crust-to-wellbore advective inflow is given in [5-6] for a Hm-scale tight gas sandstone crustal volume.

The steady-state rate at which crustal fluids flow from the crust into a wellbore, $v(x,y,z)$, is given by Darcy's law in terms of permeability distribution $\kappa(x,y,z)$ and constant dynamic viscosity of water μ,

$$v = \kappa/\mu \, \nabla P, \tag{1}$$

for appropriate fluid pressure boundary conditions in the crustal volume.

Conservation of mass requires that steady-state Darcy flow velocity has vanishing divergence, $\nabla \cdot v = 0$, yielding the defining flow equation for finite-element solvers,

$$\nabla \cdot (\kappa(x,y,z) \nabla P(x,y,z)) = 0. \tag{2}$$

The finite element method for solving differential equations allows for essentially arbitrary spatial variation of material properties such as $\kappa(x,y,z)$ [30-32]. As illustrated in Figure 4, our application of this finite element solver capability assumes that a single global numerical mesh spans the entire flow model.

If Darcy fluid flow carries heat through a medium of mean porosity ϕ, the combined steady-state conducted and advected heat energy flow is

$$\mathbf{q} = K \nabla T(x,y,z) - \varrho C \phi v(x,y,z) T(x,y,z), \tag{3}$$

for K = Fourier's thermal conductivity for rock and ϱC = fluid volumetric heat capacity. Conservation of steady-state thermal energy, $\nabla \cdot \boldsymbol{q} = 0$, then couples the spatially-variable temperature field $T(x,y,z)$ to the spatially-variable Darcy fluid velocity flow field $v(x,y,z)$ for the

Preprints (www.preprints.org) | NOT PEER-REVIEWED | Posted: 18 September 2017 doi:10.20944/preprints201709.0079.v1

Peer-reviewed version available at Energies 2017, 10, 1979; doi:10.3390/en10121979

given crustal temperature and fluid pressure boundary conditions. This coupling leads to the defining steady-state equation for a nonlinear finite-element solver,

$$\nabla\cdot\nabla T(x,y,z) = \varrho C/K\ \nabla\cdot(\phi v(x,y,z)T(x,y,z)) = 1/D\ \phi v(x,y,z)\cdot\nabla T(x,y,z), \qquad (4)$$

where the conservation of mass condition $\nabla\cdot v = 0$ is observed, and $D = K/\varrho C \sim 0.7\cdot10^{-6}\mathrm{m}^2/\mathrm{s}$ is the essentially constant thermal diffusivity of the rock-fluid system for rock thermal conductivity $K \sim 3$ W/m·°C and fluid volumetric heat capacity $\varrho C \sim 4.28\mathrm{MJ/m^3\cdot{}^\circ C}$.

Where long-range spatially-correlated fracture-connectivity percolation networks intersect a wellbore, Darcy flow can be approximated as essentially wellbore-centric radial, $v(x,y,z) \sim v(r) \sim v(r_0)r_0/r$. The 3D steady-state flow condition (4) then reduces to a 2D analytical form in wellbore-centric radius r,

$$T(r) = T_0 + (T_1 - T_0)\ ((r/r_0)^{Pe} - 1)\ /\ ((r_1/r_0)^{Pe} - 1), \qquad (5)$$

given in terms of radial flow boundaries at $r_0 < r_1$ characterized by boundary temperatures T_0 and T_1, with Peclet number $P_e = r_0\phi v_0/D$ (Appendix A). Analytic expression (5) serves to check 3D solutions of non-linear thermal energy conservation constraint equation (4), while at the same time yielding an estimate of advective fluid flow rate for the crustal fracture-connectivity flow system, $\phi v_0 \sim P_e D/r_0$.

The degree of advection heat transport relative to conductive heat transport for a given model flow structure determines the shape to the axial temperature along the wellbore. Matching the observed axial temperature profile in turn constrains the effective steady-state flow velocity of the crustal fluid leaking into the wellbore without having to know explicitly the permeability or pressure boundary conditions. Modeling axial temperature profiles interpreted as sequences of 2D wellbore-centric radial flow Peclet numbers thus has the potential to calibrate EGS wellbore-centric flow stimulation processes.

We use Matlab 3D partial differential equation solvers to model steady-state axial temperature profiles constrained by the mass conservation (2) and heat energy conservation (4). The Matlab 3D solvers [32] have two forms for a scalar field variable $u(x,y,z)$,

$$-\nabla\cdot(c(x,y,z)\nabla u(x,y,z)) + a(x,y,z)u(x,y,z) = f(x,y,z), \qquad (6)$$

and

$$-\nabla\cdot(c(x,y,z,u,u_x,u_x,u_z)\nabla u) + a(x,y,z,u,u_x,u_x,u_z)u = f(x,y,z,u,u_x,u_x,u_z). \qquad (7)$$

Eq (6) is equivalent to an elliptical partial differential equation, and (7) generalises (6) by allowing coefficients terms $c(x,y,z)$ and $a(x,y,z)$ and source term $f(x,y,z)$ to depend on the field variable $u(x,y,z)$ and its spatial derivatives, u_x, u_x and u_z. The key feature of finite-element modelling employed here is its tractability to essentially arbitrary position-dependent coefficients, e.g., $c(x,y,z)$ for (6), and $c(x,y,z,u,u_x,u_x,u_z)$ for (7), to meet the conditions imposed by stochastic poroperm media [30-32].

Preprints (www.preprints.org) | NOT PEER-REVIEWED | Posted: 18 September 2017 doi:10.20944/preprints201709.0079.v1

Peer-reviewed version available at *Energies* **2017**, *10*, 1979; doi:10.3390/en10121979

Figure 6 pictures the model geometry for wellbore-centric flow/transport simulation of Figure 2 OTN1 temperature data. Internally, the model volume is characterized by a spatially-correlated stochastic distribution of porosity $\phi(x,y,z)$ and its associated permeability field $\kappa(x,y,z) \sim \exp(\alpha\phi(x,y,z))$. The crustal volume has essentially uniform pressure and temperature conditions on each side; zero-flux boundary conditions are set on the top and bottom faces. As illustrated in Figure 4 for 2D, we can inset at will in the Figure 6 crustal volume geometric flow structures to give enhanced percolation via greater fracture connectivity along the flow structure. Where inserted flow structures intersect the model volume external boundaries, we assume the structures connect to the surrounding crust to deliver heat energy at the external boundary. As displayed in Figure 8 below, the external crustal heat energy is represented by a fixed temperature increment at the intersection of the flow structure with the model external faces.

Solutions to constraint conditions (6)-(7) determine how the incremental heat energy at the model external surfaces is expressed as temperature along the internal wellbore. In matching computed temperature profiles to observed Figure 2 temperature events, we provide a physical description of the fluid flow and heat transport process between the central wellbore and the enclosing crustal volume. By calibrating this model to OTN1 temperature events, we can explore hypothetical scenarios of EGS stimulation in which high pressure wellbore fluids enter into existing and/or relic fracture-connectivity structures in the surrounding crust.

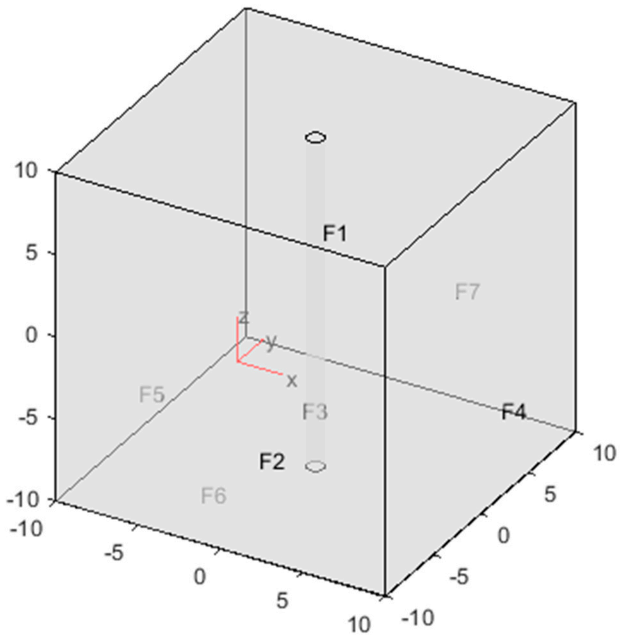

Figure 6. Wellbore-centric computational volume data cube 161 nodes on a side for node spacing ~ 12cm. A 30cm radius wellbore is denoted by shaded vertical shaft with interior surface face F3. External boundary faces are F1-F2 and F4-F7. Pressure, temperature, and/or flux boundary conditions at faces F1-F7 define the steady-state flow/advection simulation performed by Matlab finite-element solvers (6) and (7).

The scalar field variables represented by finite element scale field $u(x,y,z)$ are, for (6), pressure $P(x,y,z)$, for solving the Darcy flow constraint equation (2), and, for (7), temperature $T(x,y,z)$, for solving the thermal energy constraint equation (4). For pressure fields $u = P(x,y,z)$, (6) is used with coefficient term $c(x,y,z)$ representing permeability $\kappa(x,y,z)$, with coefficient term $a(x,y,z)$ and source term $f(x,y,z)$ set to zero. For temperature fields $u = T(x,y,z)$, (7) is used with coefficient term $c(x,y,z,u,u_x,u_x,u_z)$ set to unity, coefficient term $a(x,y,z,u,u_x,u_x,u_z)$ set to zero, and source term set to the advective flow of heat, $f(x,y,z,T,T_x,T_x,T_z) = 1/D\ \underline{\phi} v(x,y,z)\cdot\nabla T(x,y,z)$.

The Figure 6 computation volume is discretized by 161 nodes on a side. With a notional physical dimension of 20 meters per side, the nodal spatial resolution is $\Delta x = \Delta y = \Delta z = 12.5$ cm. Ambient poroperm properties within the crustal domain are numerical realisations of a 3D stochastic spatial connectivity distribution representing porosity $\phi(x,y,z)$ and associated permeability $\kappa(x,y,z) \sim \exp(\alpha\phi(x,y,z))$ given by crustal empirics (I)-(III). Figure 7 shows the degree of spatial heterogeneity typical of the power-law scaling spatial fluctuation amplitudes: ~ 6 octaves for the normally distributed porosity about mean porosity $\underline{\phi} \sim 1.2\%$ and ~ 9 octaves for the lognormally distributed permeability generated by fracture-connectivity parameter $\alpha \sim 300$.

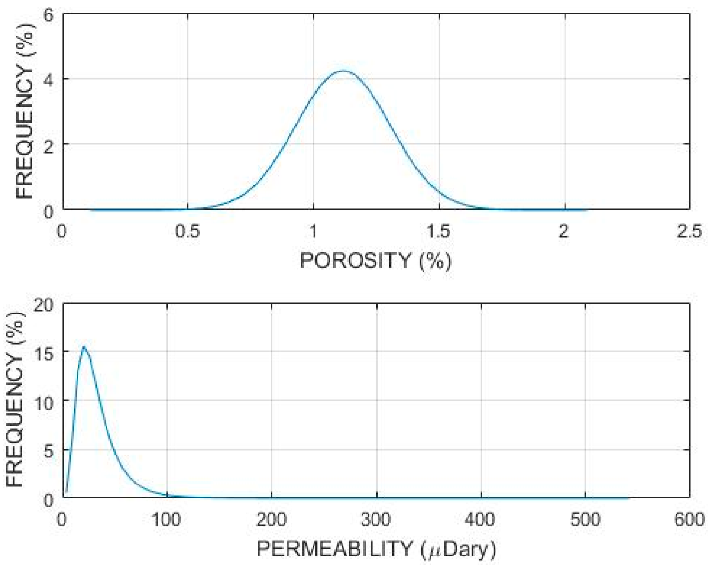

Figure 7. Frequency distributions typical of ambient porosity and permeability fluctuations embedded in Figure 6 numerical crustal volume characterized by spatially correlated porosity and permeability empirics (I)-(III).

The wellbore interior boundary surface is assigned a boundary flux distribution. As our modelling task is to compute an interior temperature distribution on the basis of an exterior temperature distribution, we assign the wellbore a heat flux boundary condition which generates an associated temperature distribution $T_0(r_0,z) = 1/h\ q_0(r_0,z)$ on the basis of the computed heat delivered to the wellbore. For present purposes, the heat transfer coefficient h is taken to be a free model parameter.

Model wellbore radii can range from a 5-node diameter (30cm radius) as in Figure 6 to a 50-node diameter (3m radius) as in Figure 14 below. Modelling with a range of wellbore radii within the numerical volume checks for possible effects of a small wellbore defined by few nodes, and possible effects on wellbore axial temperature distribution due to the radial distance over which fluids travel from the exterior crustal boundary to the interior wellbore boundary.

To compute Darcy flow velocity $v(x,y,z)$, the wellbore is assumed to be at hydrostatic pressure. Fluid in the crustal volume will be subject to higher pressure, most probably given by the minimum principal stress. Given the fluid-flow empirics (I)-(III), almost all fluid will ultimately be connected through a global fracture-connectivity pathway, and hence the fluid pressure will be approximately in equilibrium with the minimum principal stress. As the minimum horizontal principal stress, σ_h ~ 22MPa/km · zkm, exceeds hydrostatic pressure, P_h ~ 10MPa/km · zkm, wherever in the crustal volume there is a geometric feature of elevated fracture-connectivity parameter α that connects the surrounding crust to the interior wellbore, we can assume that fluid pressure σ_h outside the model cube drives fluid from the crust into the wellbore. In consideration of wellbore temperature log data in Figures 1-2 and illustrative 2D heat transport modelling of Figure 4, we can suppose that over time episodes of fluid flow in the wellbore have removed heat from the wellbore and its immediately proximate crust [5-6]. It follows that fracture-connectivity pathways leaking fluid into the wellbore bring crustal heat into the wellbore to generate positive temperature events at sites where fracture-connectivity structures intersect the wellbore (e.g., Figure 4).

A model external boundary temperature distribution is illustrated in Figure 8. The incremented boundary temperature field corresponds to a 0.6m-thick horizontal flow structure of higher poro-connectivity parameter α which conveys fluids from the surrounding crustal volume to the central wellbore. Figures 9-10 display quadrant section contour plots for the temperature and heat transport solutions to (7) generated by the 0.6m-thick flow structure pictured in Figure 8. Figure 11 shows model wellbore axial temperature profile matches for the Figure 2 significant OTN1 temperature events in the 1120m-1700m interval of granite basement. Except for the upper-right temperature event of Figure 11, the Figure 8-10 model flow structures have 0.6m thicknesses. A 2-3m thickness flow structure is required to match the 1405m-depth temperature event shown in the Figure 11 upper-right profile.

 doi:10.20944/preprints201709.0079.v1

Peer-reviewed version available at *Energies* **2017**, *10*, 1979; doi:10.3390/en10121979

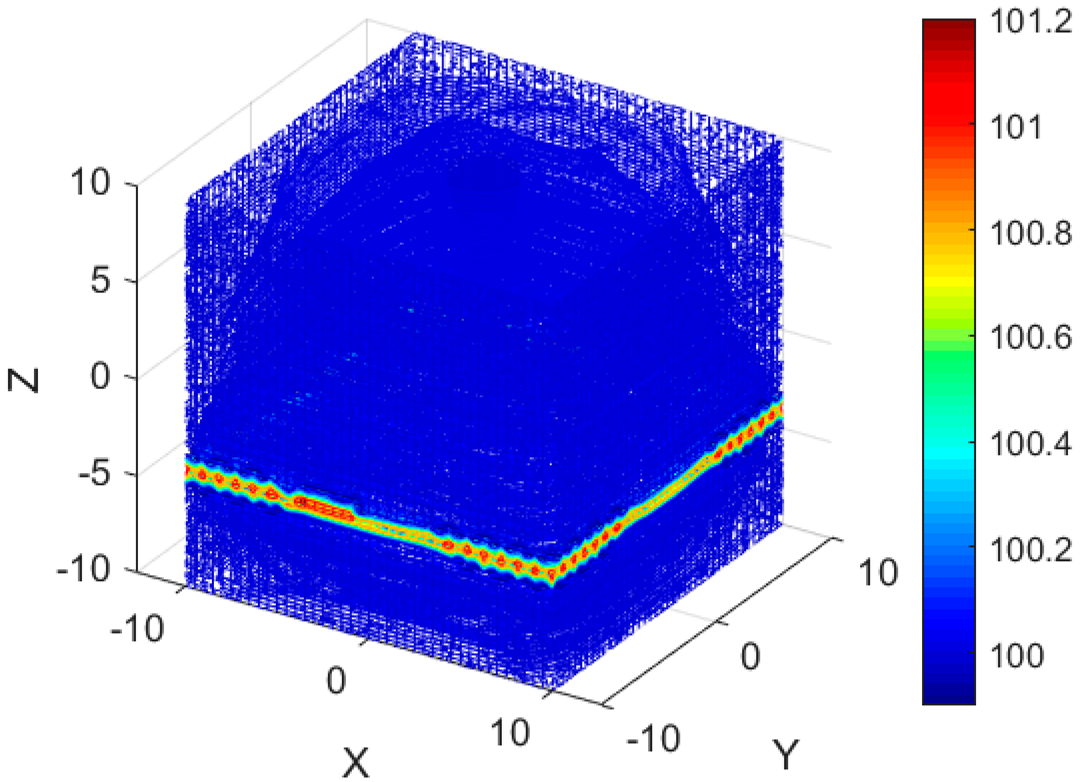

Figure 8. Model crustal volume external boundary temperature distribution over wellbore-centric computational volume for 0.6m-thick fracture-connectivity fluid flow horizon that intersects an internal vertical wellbore. Following Figure 6, the model volume is 20m on a side and with an embedded central vertical wellbore. By model hypothesis, the crustal volume is at a constant ambient fluid pressure and temperature (nominally 100^{o}C), with the interior wellbore at lower fluid pressure and temperature. A horizonal crustal section of elevated poro-connectivity permeability $\kappa(x,y,z) \sim \exp(\alpha\phi(x,y,z))$ feeds fluid of incrementally higher temperature through the model volume into the wellbore. The elevated model boundary temperature is fixed at nominal 1^{o}C above the ambient temperature. Steady-state fluid inflow from the crust at incremented boundary temperature transports heat to the wellbore, creating a localized temperature deviation from the ambient wellbore temperature. With these boundary conditions, the steady-state finite-element solver (7) generates a 3D temperature field that obeys the conservation of energy constraint equation (4). The model axial temperature distribution at the central wellbore is compared to OTN1 temperature profiles in Figure 2. The resulting 3D temperature field is nominally a series of radially symmetric wellbore-centric temperature distributions that vary as a function of depth along the wellbore. The finite-element model 2D approximations to wellbore-centric temperature distributions can be compared with the analytic solution (5) for strictly 2D wellbore-centric flow characterized by Peclet number $P_e = r_0\phi v_0/D$.

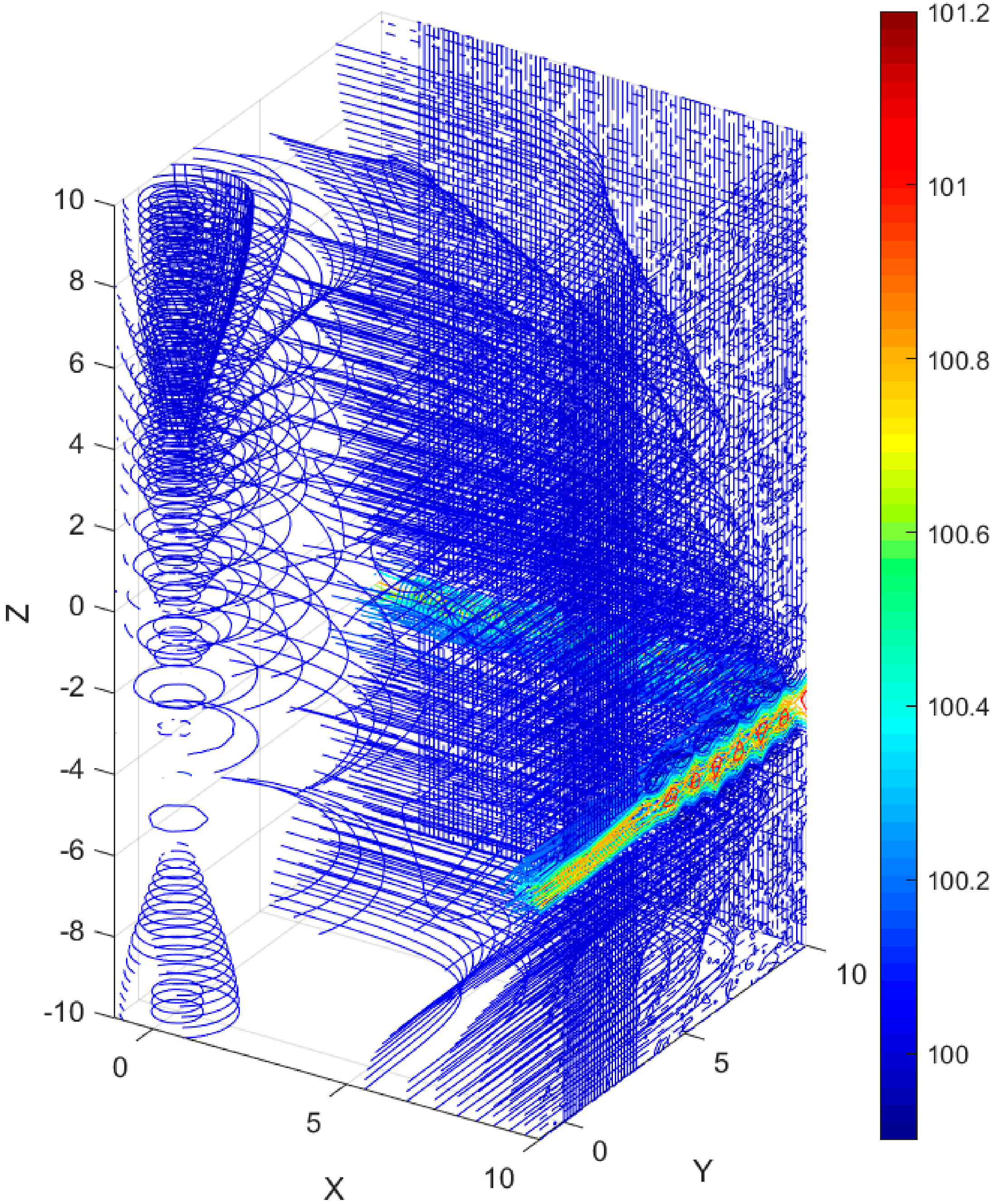

Figure 9. Quarter section of temperature distribution over wellbore-centric computational volume for thin fracture-connectivity plane illustrated in Figure 8. Wellbore axis is located at (x,y) = (0,0). Model dimensions in meters. Model temperatures are nominal 100°C with 1°C of elevated temperature at z = 4 horizon of advective flow entry from enclosing crustal volume.

Preprints (www.preprints.org) | NOT PEER-REVIEWED | Posted: 18 September 2017 doi:10.20944/preprints201709.0079.v1

Peer-reviewed version available at Energies 2017, 10, 1979; doi:10.3390/en10121979

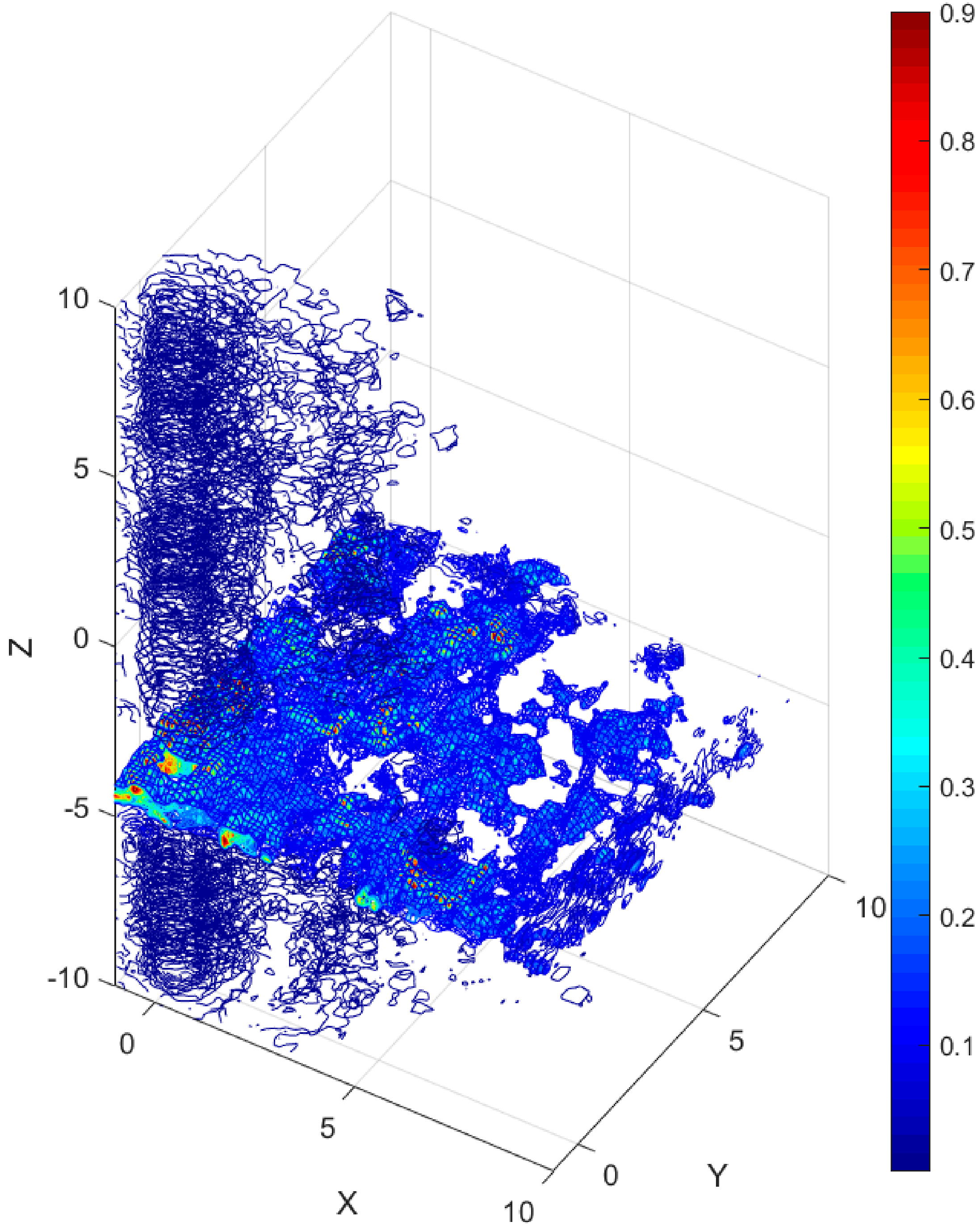

Figure 10. Quarter section of normalised advective heat flow distribution over wellbore-centric computational volume for thin fracture-connectivity plane illustrated in Figure 8. The temperature field associated with the displayed advective flow distribution is shown in Figure 9. Wellbore axis is located at (x,y) = (0,0). Model dimensions in meters.

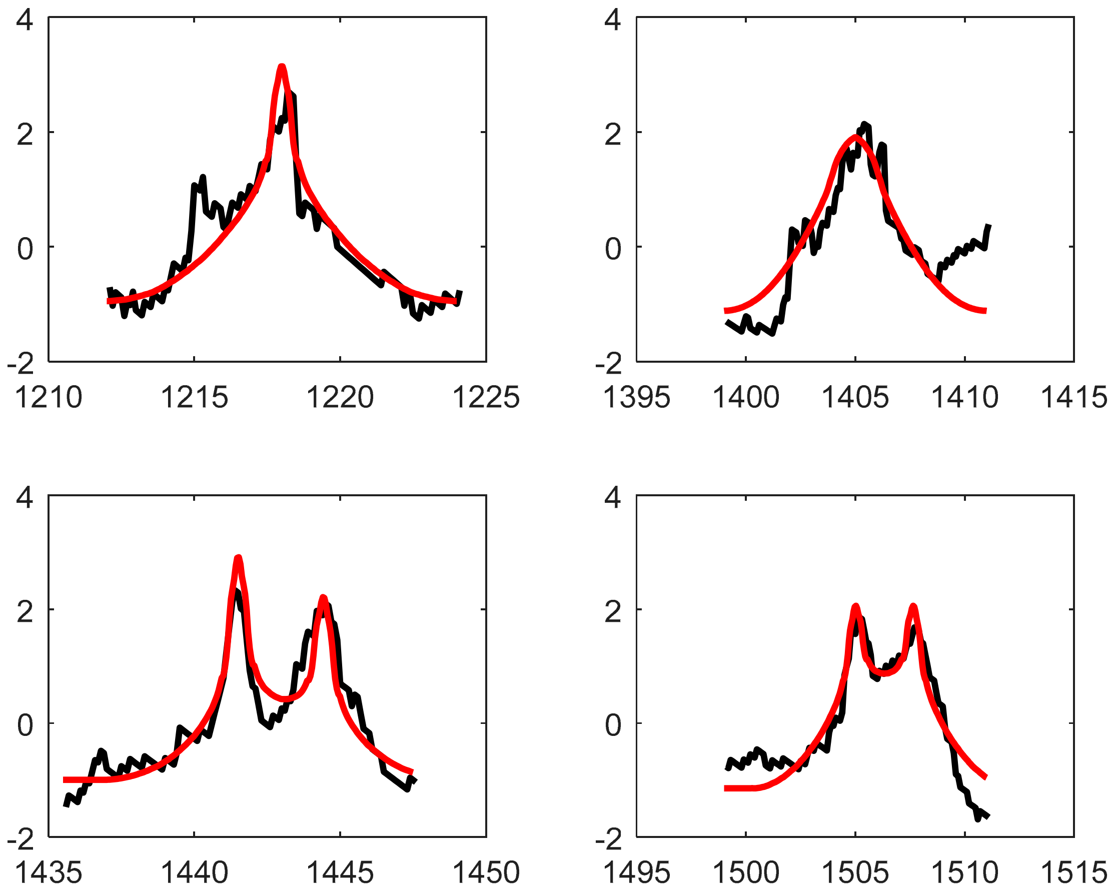

Figure 11. Overlays of Figure 6 model wellbore axial temperature profiles (red traces) for 30cm radius wellbore embedded in a 10-meter radius crustal volume superposed on OTN1 wellbore temperature inflexions (black traces). Horizontal axes give wellbore depth in meters; vertical axes are temperature distributions normalised to zero-mean/unit-variance format. The favoured model flow channel thickness is 0.6m, as illustrated in Figure 8. The observed flow channel events occur either singly or in pairs. (Upper left) Model temperature profile computed for single 0.6m thick flow channel. (Upper right) Model temperature profile for 2-3m thick flow channel. (Lower left) Model temperature profile for 4-m spaced pair of 0.6m thick flow channels. (Lower right) Model temperature profile for 3-m spaced pair of 0.6m thick flow channels.

The Figure 11 advection flow model wellbore temperature profiles computed by (7) for Figure -8-like flow-structure geometry and boundary conditions provide plausible shapes to fit to the Figure 2 observed OTN1 wellbore temperature profiles. Agreement between the model and observed profiles indicate that axial temperature diffusion by conduction combined with radial advective heat transfer via 0.6-m-thick flow structures into a 30cm-radius wellbore provide reasonable approximations to the diffusion-advection process hypothesized for fracture-connectivity fluid percolation structures observed in Fennoscandia basement rock at depths to 2.5 km.

Preprints (www.preprints.org) | NOT PEER-REVIEWED | Posted: 18 September 2017 doi:10.20944/preprints201709.0079.v1

Peer-reviewed version available at Energies 2017, 10, 1979; doi:10.3390/en10121979

4. 2D wellbore-centric radial flow Peclet number characterization of 3D temperature models

Figures 8-11 describe the steady-state 3D wellbore-centric temperature field around a vertical wellbore when heat-transporting fluid flows into the wellbore from horizontal flow structures as given in Figure 8. For wellbore levels at or near horizonal flow structures, the radial temperature distribution is dominated by thermal advection (high Peclet numbers), while at wellbore axial offsets away from horizontal flow structures, the radial temperature field is dominated by thermal conduction (low Peclet numbers).

Figure 12 shows the axial changes in model radial temperature profiles (blue dots) for the 1218m OTN1 temperature event given in the upper left plot of Figure 11. Model radial temperature profiles $T_0 < T(r) < T_1$ for $r_0 < r < r_1$ at successive depths along the wellbore axis are approximated by best-fits (red traces) to steady-state radial temperature distribution (5) for free parameter Peclet number $P_e = r_0 \phi v_0 / D$,

$$T(r) = T_0 + (T_1 - T_0)\,((r/r_0)^{Pe} - 1) / ((r_1/r_0)^{Pe} - 1), \qquad (5)$$

as the Darcy flow heat transport rates ϕv_0 vary with depth along the wellbore interval in crustal rock of mean porosity ϕ and thermal diffusivity $D \sim 0.7 \cdot 10^{-6} m^2/s$ (Appendix A).

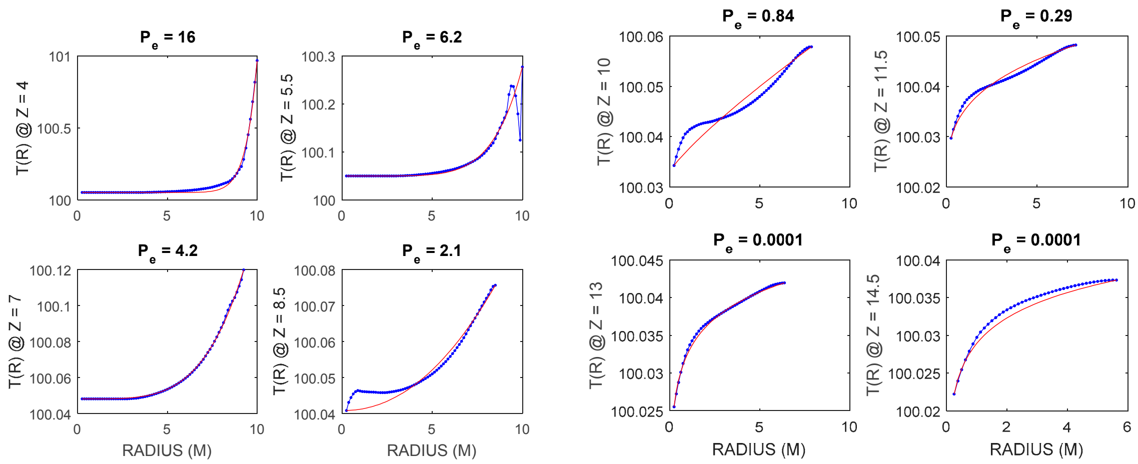

Figure 12. 2D analytic wellbore-centric radial temperature profiles (red traces) for given Peclet number superposed on 3D numerical model radial temperature distributions (blue dots) for 30cm radius wellbore embedded in 10-meter radius crustal volume as seen in Figure 8. Horizontal axes are wellbore-centric radius in meters; vertical axes are temperatures from nominal wellbore ambient $T_0 \sim 100$ to ambient crust $T_1 \sim 100^oC + \Delta T$ for $\Delta T \sim 0.05^oC$ except near the advective flow horizon when $\Delta T = 1^oC$. From upper left of left quartet to lower right of right quartet, the 3D model radial temperature distributions are fit to 2D steady-state radial temperature distributions (5) governed by numbers $P_e = r_0 \phi v_0 / D$. The Peclet number for the fracture-connectivity horizon is 16. Stepping away from the horizon in 1.5m intervals, the Peclet numbers decline as 6.2, 4.2, and 2.1. At wellbore axial offsets greater than 6m from the fracture-connectivity horizon, thermal conductivity values of Peclet numbers $P_e < 1$ dominate.

Preprints (www.preprints.org) | NOT PEER-REVIEWED | Posted: 18 September 2017 doi:10.20944/preprints201709.0079.v1

Peer-reviewed version available at Energies 2017, 10, 1979; doi:10.3390/en10121979

Figure 12 assumes an ambient wellbore temperature T_0 ~ 100°C and external ambient crustal temperature T_1 ~ 100°C + ΔT, ΔT ~ 0.05°C except near the advective flow horizon when ΔT = 1°C. Eq (5) is fit to the Figure 9 numerical model radial temperature distributions for the sequence of wellbore depths. Beginning at the upper-left plot, successive axial offsets from the horizontal fracture-connectivity flow structure are described by decreasing Peclet numbers as thermal advection heat transfer decreases relative to thermal conduction heat transfer. The 2D analytic approximations (5) for optimized Peclet number closely fit the numerical model temperature profiles. The Figure 12 agreement between a sequence of 2D analytic expression (5) optimized for Peclet number, and the Figures 8-11 3D numerical model temperature distribution validates the finite-element numerical procedure (7). Figure 13 characterizes the effective Darcy fluid inflow parameter $\phi v_0 = P_e D/r_0$ at offsets along the wellbore axis from the advective heat inflow horizon.

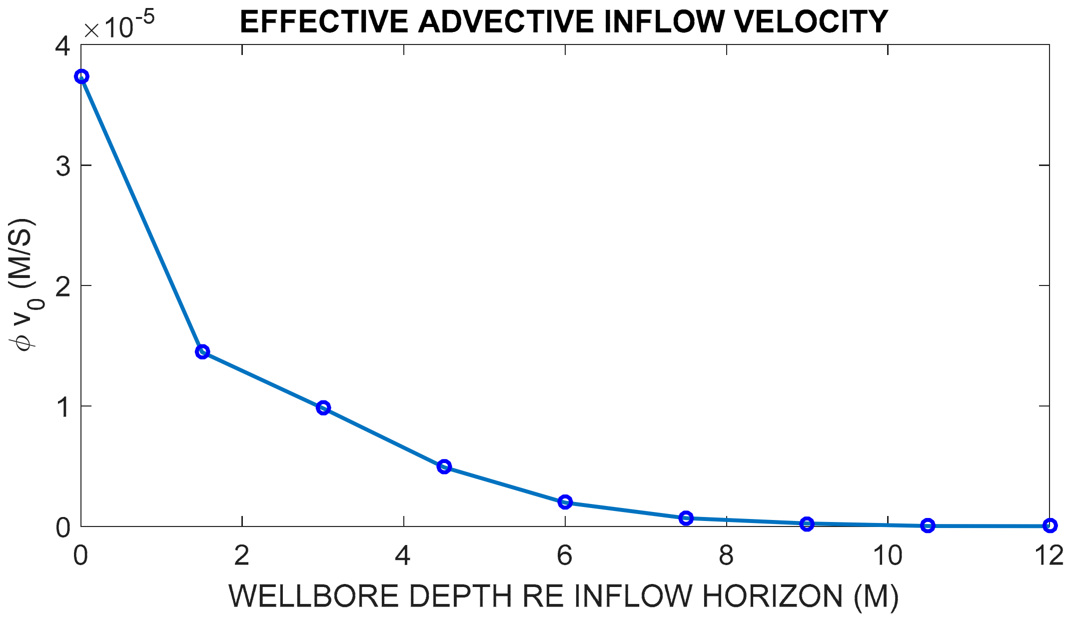

Figure 13. Effective inflow velocity $\phi v_0 = P_e D/r_0$ at successive wellbore offsets from the inflow horizon given by the Figures 8-12 model of OTN1 temperature event at depth 1218 meters. For crustal rock of mean porosity ϕ = 0.01, the computed inflow Darcy fluid velocity at wellbore radius 30cm is v_0 ~ 4 mm/s across a 1m wellbore depth interval.

The relation of wellbore-centric model Peclet numbers in Figure 12 to axial temperature profiles in Figure 11 is governed in part by the ratio of the inner and outer model radii r_1/r_0. The heat advection flow computation for Figures 8-13 assumes model radius r_1 = 10m enclosing a wellbore radius r_0 = 30cm, giving model/wellbore radius ratio r_1/r_0 = 33. The steady-state advective heat transfer temperature field (5) indicates that for Peclet numbers of interest, e.g. P_e > ~3, wellbore-centric heat transfer for large values of r_1/r_0 is essentially decoupled from the external boundary. As we are primarily interested in interpreting wellbore axial temperature events in terms of fluid inflow from crustal domain fracture-connectivity structures, we look at the degree of spatial resolution that the Figure 2 OTN1 wellbore temperature events can give for the scale of flow structures away from the wellbore.

Preprints (www.preprints.org) | NOT PEER-REVIEWED | Posted: 18 September 2017 doi:10.20944/preprints201709.0079.v1

Peer-reviewed version available at Energies 2017, 10, 1979; doi:10.3390/en10121979

While the steady-state heat flux temperature field (5) formally returns a value T_1 for radius $r=r_1$ for all values of Peclet number P_e, for radii much larger than the wellbore radius but smaller than the model radius, $r_0/r_1 \ll r/r_1 < 1$, (5) reduces to

$$T(r_0/r_1 \ll r/r_1 < 1) \sim T_0(1 - (r/r_1)^{Pe}) + T_1 (r/r_1)^{Pe} \sim T_0 + T_1(r/r_1)^{Pe}. \quad (8)$$

For values of the model exterior temperature T_1 differing little from the wellbore temperature T_0, $T(r) \sim T_0$ for most of the radial extent away from the wellbore, and as a result the value of the external boundary temperature T_1 has little influence on the wellbore temperature profile.

Expressing system steady-state advective heat flow (3) in terms of (5) gives,

$$q(r) \sim KP_e/r\ (T_1 - T_0)(r_0/r_1)^{Pe} - T_0, \quad (9)$$

from which the wellbore temperature T_0 is directly dependent on the crustal heat inflow q_1 at the model external boundary,

$$T_0 \sim T_1(r_0/r_1)^{Pe} - r_1 q_1/KP_e. \quad (10)$$

While (10) is analytically straightforward, for numerical solutions it is preferable to give a temperature rather than a heat flux boundary condition. We can, accordingly, use (10) to infer the magnitude of the heat influx at the model boundary from the given numerical value of the wellbore temperature T_0.

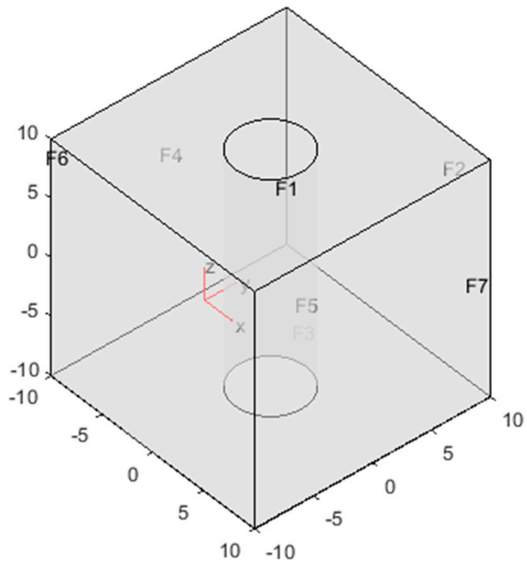

Figure 14. Following Figure 6, a wellbore-centric data cube of 161 nodes with node spacing ~ 12cm and a 3m radius wellbore denoted by shaded vertical shaft with interior surface face F5. External boundary faces are F1-F4 and F6-F7. Pressure, temperature, and/or flux boundary conditions at faces F1-F7 define the steady-state flow/advection simulation performed by Matlab finite-element solvers (6) and (7).

The physical and numerical implications of (8)-(10) motivate examining the model wellbore temperature profile for a smaller model/wellbore radius ration, $r_1/r_0 = 3$ (Figure 14). Computing

Peer-reviewed version available at Energies 2017, 10, 1979; doi:10.3390/en10121979

the axial temperature profile for a model wellbore radius r_0 = 3m in an r_1 = 10m model volume tests the extent to which the r_1/r_0 influences model axial temperature distributions. The Figure 15 results of the Figure 14 wellbore model are to be compared with Figure 11.

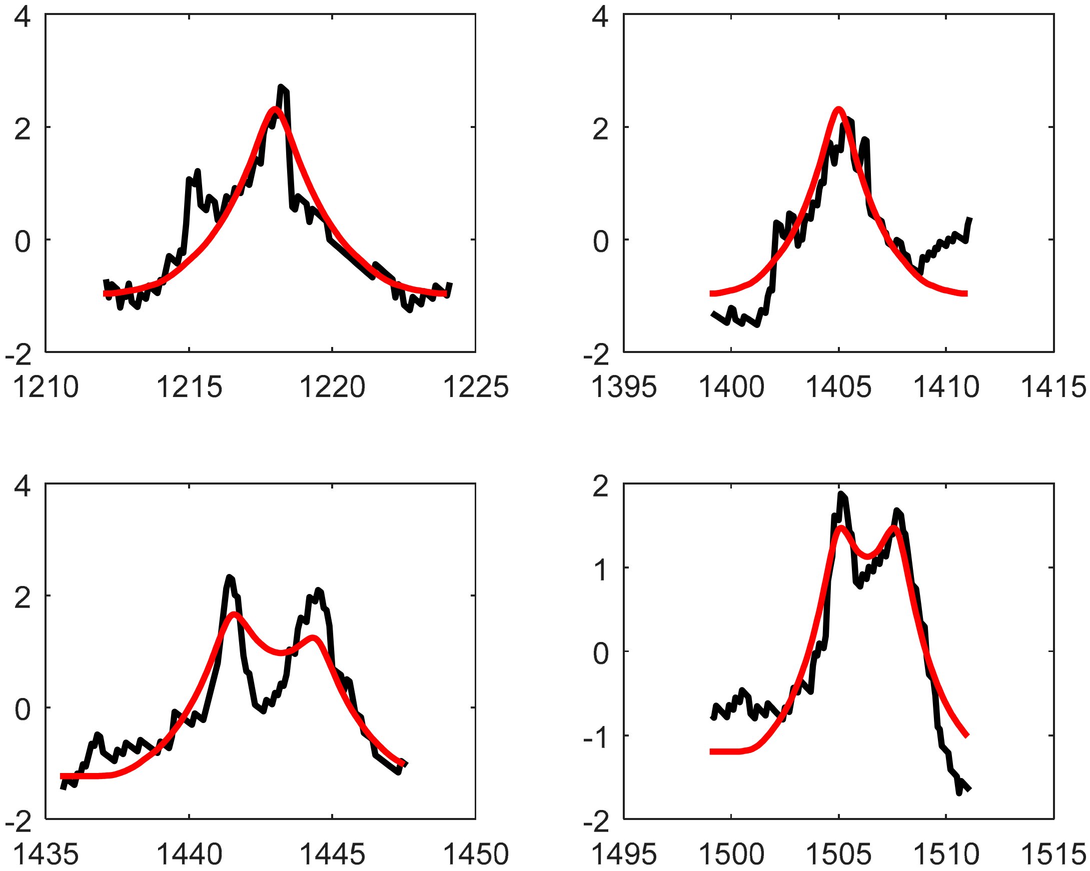

Figure 15. Following Figure 11, overlays of Figure 14 model wellbore axial temperature profiles (red traces) for 3m radius wellbore embedded in a 10-meter radius crustal volume superposed on OTN1 wellbore temperature inflexions (black traces). Horizontal axes give wellbore depth in meters; vertical axes are wellbore temperature profiles normalised to zero-mean/unit-variance. The favoured model flow channel thickness is 0.6m, as illustrated in Figure 8. (Upper left) Model temperature profile computed for single 0.6m thick flow channel. (Upper right) Model temperature profile for 2-3m thick flow channel. (Lower left) Model temperature profile for 4-m spaced pair of 0.6m thick flow channels. (Lower right) Model temperature profile for 3-m spaced pair of 0.6m thick flow channels.

Figure 11 versus Figure 15 model fits to OTN1 wellbore axial temperature profiles quantifies the effect of an order of magnitude wellbore/model radius ratio r_1/r_0 difference, 33 to 3.3. For 0.6m thick advective fluid inflow fracture-connectivity horizons, the 30cm wellbore temperature profiles are more sharply peaked than the 3m wellbore temperature profiles. In particular, the lower panels of Figures 11 and 15 show that model temperature profiles for adjacent 0.6m inflow horizons follow the observed temperature contours for a 30cm wellbore while model profiles for a 3m wellbore cannot follow these contours. We conclude on the basis of the latter condition that 0.6m-

Preprints (www.preprints.org) | NOT PEER-REVIEWED | Posted: 18 September 2017 doi:10.20944/preprints201709.0079.v1

Peer-reviewed version available at Energies 2017, 10, 1979; doi:10.3390/en10121979

thick fracture-connectivity inflow structures draining into an r_0 = 30cm wellbore must extend deeper into the crust than r_1 = 1 meter.

Figures 16-17 indicate that a 1m radius wellbore model, $r_1/r_0 = 10$, does not match the OTN1 temperature profile for the adjacent inflow horizons shown in the lower-left panel of Figure 17. The 1m model wellbore matches the lower-right panel better than does the 3m model wellbore but does not require a narrower gauge wellbore model. From the Figures 11, 15, and 17 model/data matches, we can infer that, within the limits of our 161-node 3D computational spatial resolution, crustal penetration of a 0.6m-thick fracture-connectivity inflow structures is greater than 3 meters and is consistent with being a great as 10 meters.

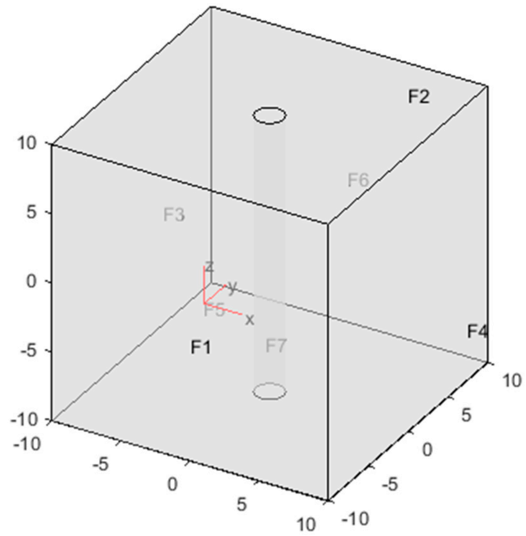

Figure 16. Following Figures 6 & 14, a 1m radius wellbore denoted by shaded vertical shaft with interior surface face F7.

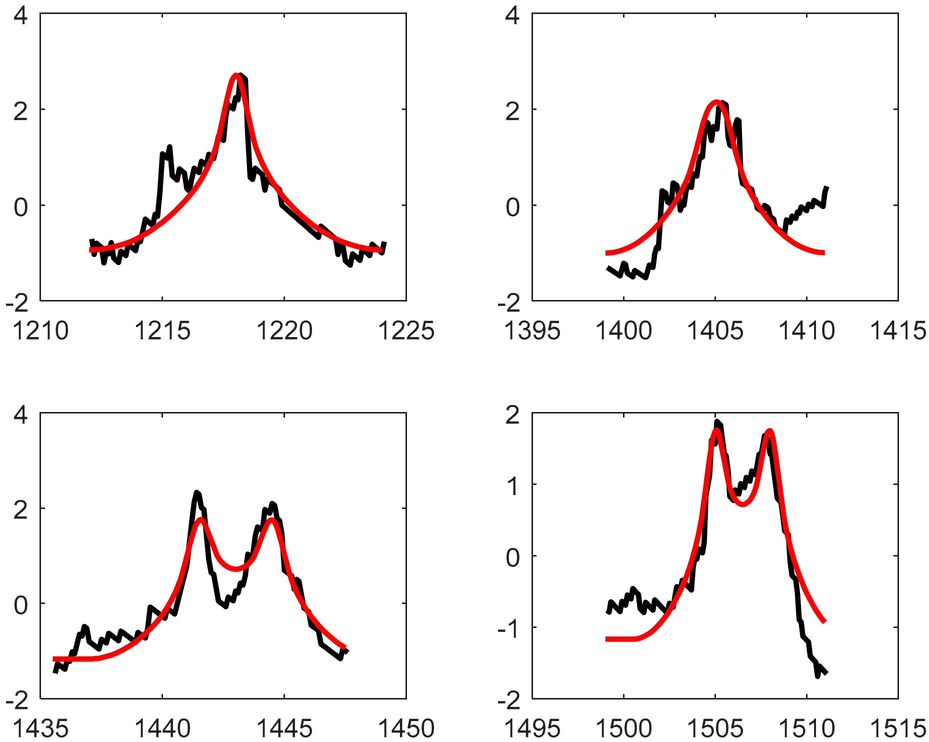

Figure 17. Following Figures 11 & 15, overlays of Figure 16 model wellbore axial temperature profiles (red traces) for 1m radius wellbore embedded in a 10-meter radius crustal volume superposed on OTN1 wellbore temperature inflexions (black traces). (Upper left) Model temperature profile computed for single 0.6m thick flow channel. (Upper right) Model temperature profile for 2-3m thick flow channel. (Lower left) Model temperature profile for 4-m spaced pair of 0.6m thick flow channels. (Lower right) Model temperature profile for 3-m spaced pair of 0.6m thick flow channels.

The effect of thickening the fracture-connectivity structures draining into a wellbore is illustrated in Figures 18-19 for a 1m radius wellbore. Figure 18 essentially duplicates for a 1m radius wellbore what Figure 12 shows for a 30cm radius wellbore for a 0.6m-thick inflow structure. After large Peclet numbers, $P_e \sim 15$, at the location of the inflow structure, at 10m offsets from the inflow structure effective advective heat transport is reduced to the level the level of thermal conduction, $P_e < 1$. Figure 19 shows, however, that the effect of increasing the thickness of the inflow structure to 2-3m reduces the Peclet number near the inflow structure, $P_e \sim 5$, and extends the axial effect of heat advective flow beyond 10m. A thick advective heat influx structure spreads the axial temperature profile along the wellbore. The axial temperature spreading effect seen in the Peclet numbers of Figure 19 corresponds to the broader OTN1 temperature event pictured in the upper-right panels of Figures 11, 15 and 17.

Preprints (www.preprints.org) | NOT PEER-REVIEWED | Posted: 18 September 2017 doi:10.20944/preprints201709.0079.v1

Peer-reviewed version available at *Energies* **2017**, *10*, 1979; doi:10.3390/en10121979

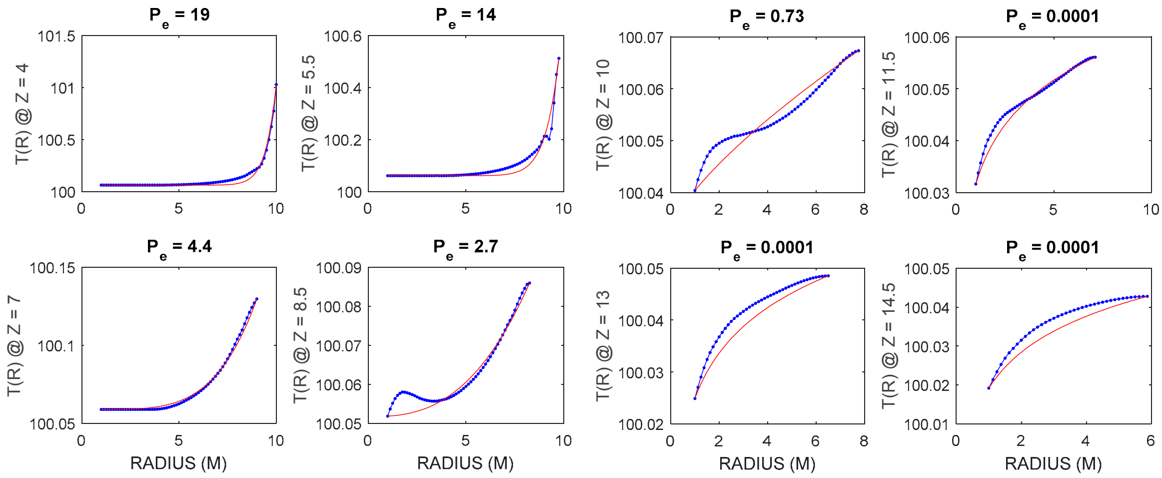

Figure 18. Following Figure 12, 2D analytic wellbore-centric radial temperature profiles (red traces) for given Peclet number superposed on 3D numerical model radial temperature distributions (blue dots) for 1m radius wellbore embedded in 10-meter radius crustal volume (Figure 16) with a 0.6m fracture-connectivity structure. From upper left of left quartet to lower right of right quartet, the 3D model radial temperature distributions are fit to 2D steady-state radial temperature distributions (5) governed by numbers $P_e = r_0 \phi v_0/D$. The Peclet number for the fracture-connectivity horizon is of order 14-19. Stepping away from the horizon in 1.5m intervals, the Peclet numbers decline as 4.4, 2.7, and 0.7.

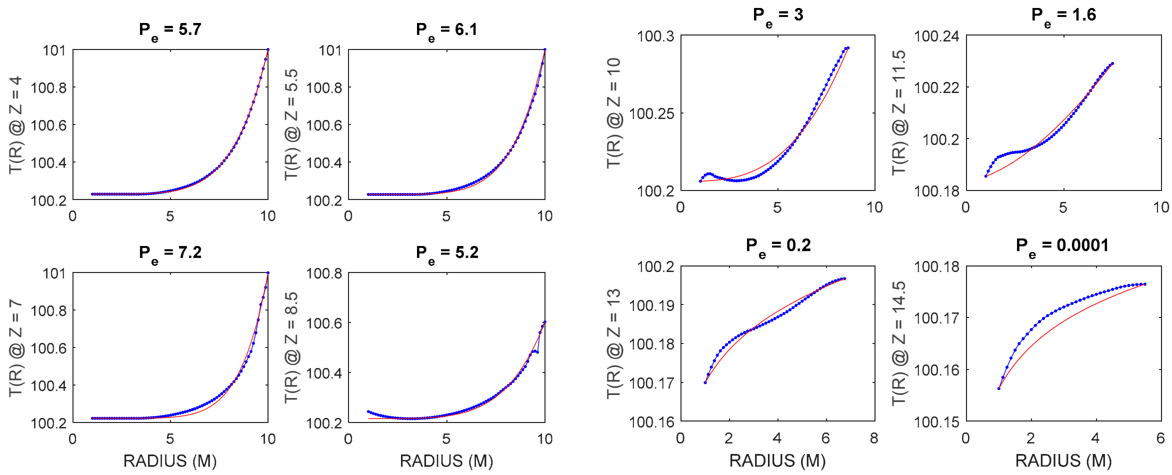

Figure 19. Following Figure 18, 2D analytic wellbore-centric radial temperature profiles (red traces) for given Peclet number superposed on 3D numerical model radial temperature distributions (blue dots) for 1m radius wellbore embedded in 10-meter radius crustal volume with a 2-3m fracture-connectivity structure. From upper left of left quartet to lower right of right quartet, the 3D model radial temperature distributions are fit to 2D steady-state radial temperature distributions (5) governed by numbers $P_e = r_0 \phi v_0/D$. The Peclet number for the fracture-connectivity horizon is 7. Stepping away from the horizon in 1.5m intervals, the Peclet numbers decline as 6.2, 4.2, and 2.1. At wellbore axial offsets greater than 6m from the fracture-connectivity horizon, thermal conductivity values of Peclet numbers $P_e < 1$ dominate.

Preprints (www.preprints.org) | NOT PEER-REVIEWED | Posted: 18 September 2017 doi:10.20944/preprints201709.0079.v1

Peer-reviewed version available at *Energies* **2017**, *10*, 1979; doi:10.3390/en10121979

From 2D steady-state wellbore-centric flow and temperature expressions (9)-(10), $r_1q_1 = r_0q_0 = KP_e\Delta T_0$ gives the rate at which heat energy leaves the model crustal volume due to radial heat flow in Peclet number $P_e \sim 10$ fracture-connectivity structures producing OTN1 temperature excursions $\Delta T_0 \sim 0.05$-0.1^oC. Advective heat energy leaving the model crustal volume via wellbore-centric fluid inflow structures of thickness ℓ is then $\Delta Q_{ad} = q_0\, 2\pi r_0\, \ell = 2\pi\, P_e K \ell \Delta T_0$. For $P_e = 10$ and $\ell = 1$m, $\Delta Q_{ad} = 2\pi\ 10\ 3$W/m/^{o}C 1m 0.1^{o}C ~ 20W for each temperature event. A similar degree of wellbore-centric heat, $\Delta Q_{cd} \sim 20$W, exits from the crustal volume due to conduction, $P_e \sim 1$, intervals of wellbore length $\ell = 10$m.

The heat energy of a crustal volume of size 10^3m^3 and heat capacity 840J/kg/^{o}C · 2200kg/m^3 at 100^{o}C ambient temperature is E = 100GJ. At an estimated 40W loss of heat energy due to OTN1 advection temperature events and associated heat conduction, the model crustal volume loses heat energy ΔE ~ 40W · $3\cdot10^7$s ~ 1.2 GJ at the rate of 1% per year. As the advectively lost heat of the OTN1 temperature events is easily replaced by thermal conduction at the model boundaries, the observed heat rate loss is consistent with a steady-state thermal condition. Advective heat flow into the model volume via a wellbore-centric flow structure occurs at a rate, $q_1 = KP_e\Delta T_0/r_1 \sim 0.3$ W/m^2, about 6 times the nominal crustal heat flow rate of 50mW/m^2.

Spatially averaged fluid flow velocity estimates proceed from model Peclet numbers, $v_0 \sim P_e D/\underline{\phi} r_0$ at the wellbore and $v_1 \sim P_e D/\underline{\phi} r_1$ at the model periphery. For a model $P_e \sim 10$ advective flow system with 10m external radius in a crustal medium of mean ambient porosity $\underline{\phi} \sim 0.01$ and thermal diffusivity D ~ $0.7\cdot10^{-6}$ m^2/s, the external crustal inflow fluid flow velocity $v_1 \sim .7\cdot10^{-4}$ m/s. From Darcy's law (1), the associated model permeability of the fracture-conductivity flow structure generating OTN1 temperature events, $\kappa_m \sim v\mu/\partial_r P$, is given by wellbore-crust pressure differential $\Delta P/\Delta r$ and fluid viscosity $\mu \sim 0.5\cdot10^{-3}$ Pa·s. Estimating the wellbore-crust pressure differential ΔP as the difference between wellbore hydrostatic pressure $P_h \sim$ 10MPa/km · 1.5km and crustal pore pressure given by the minimum principal stress $\sigma_h \sim P_p \sim$ 22MPa/km · 1.5km for crustal minimum principal stress at 1.5km depth, $\kappa_m \sim .7\ 10^{-4}$ m/s · $.5\cdot10^{-3}$ Pa·s · 10m/(12 · 1.5 · 10^6Pa) ~ $2\cdot10^{-14}$m^2 ~ 0.02Darcy. The fracture connectivity parameter associated with the fracture-connectivity flow structures generating observed temperature events is then $\kappa_m \sim \underline{\kappa}\exp(\alpha_m\underline{\phi})$ for $\underline{\phi} \sim 0.01$ and $\underline{\kappa} \sim 1\mu$Darcy is then $\alpha_m \sim 1000$. If we associate an effective ambient value for poro-connectivity $\alpha \sim 500$ (Figures 25-29 [24-27]), then an OTN1 temperature event model flow structure poro-connectivity $\alpha_m \sim 1000$ is of order twice the ambient value is nominally characteristic of Peclet number $P_e \sim 10$ flow structures.

5. Wellbore temperature event modelling as calibration of EGS stimulation of basement rock

Fennoscandia basement rock wellbore OTN1 temperature event modelling pictured in Figures 6-19 suggests a canonical or type concept of basement rock fracture-connectivity permeability that is amenable to detailed numerical investigation of wellbore-centric fluid processes in Dm-scale crustal volumes characterised by spatially-correlated poroperm distributions. Porosity spatial correlation is defined by empirical condition (I) that a wellbore porosity sequence $\phi(\xi)$ within the crustal volume has a Fourier power-spectrum $S_\phi(k)$ that scales inversely with spatial wavenumber k,

Preprints (www.preprints.org) | NOT PEER-REVIEWED | Posted: 18 September 2017 doi:10.20944/preprints201709.0079.v1

Peer-reviewed version available at *Energies* **2017**, *10*, 1979; doi:10.3390/en10121979

$S_\phi(k) \propto 1/k^\beta$, $\beta \sim 1$. The spatially-correlated normal distributions of porosity $\phi(x,y,z)$ give the associated permeability $\kappa(x,y,z) \propto \exp(\alpha\phi(x,y,z))$ fields a lognormal distribution for sufficiently large parameter α in accord with empirical conditions (II)-(III).

Our present wellbore-centric flow modelling results can be placed in a wider basement rock permeability stimulation context:

- OTN1 solute-transport galvanic well-log profiles parallel OTN1 basement rock temperature profiles.
- Deep basement well-log and well-core data supporting spatial-correlation empirics (I)-(III) imply general application to EGS basement rock stimulation.
- Crustal deformation energetics appear to favour spatially-correlated granularity over planar continuum flow structures, implying wide application of the present modelling construct.
- Wellbore-centric flow modelling provides a simple calculus for the physical scales needed for successful EGS commercial outcomes.

5.1. OTN1 basement rock solute transport events

It is plausible that the episodes of fluid influx into the OTN1 well that transport heat to the wellbore fluid also register as electrical conductivity fluctuations responding to increases solute content and/or solute transport that registers as a spontaneous potential signal. Figure 20 indicates considerable spatial correlation between the OTN1 temperature profile (black dots) and two OTN1 galvanic profiles, lateral log induction (blue trace) and spontaneous potential (red trace). As solute concentrations obey a gradient law similar to Fourier's law of heat transport, temperature modelling is similar to fluid solute concentration modelling. However, while the gradient flow principle is the same, brine concentrations are affected by local rock mineralogy with no parallel in thermal properties, hence a one-to-one correspondence between temperature and solute wellbore fluid inflow events is not expected.

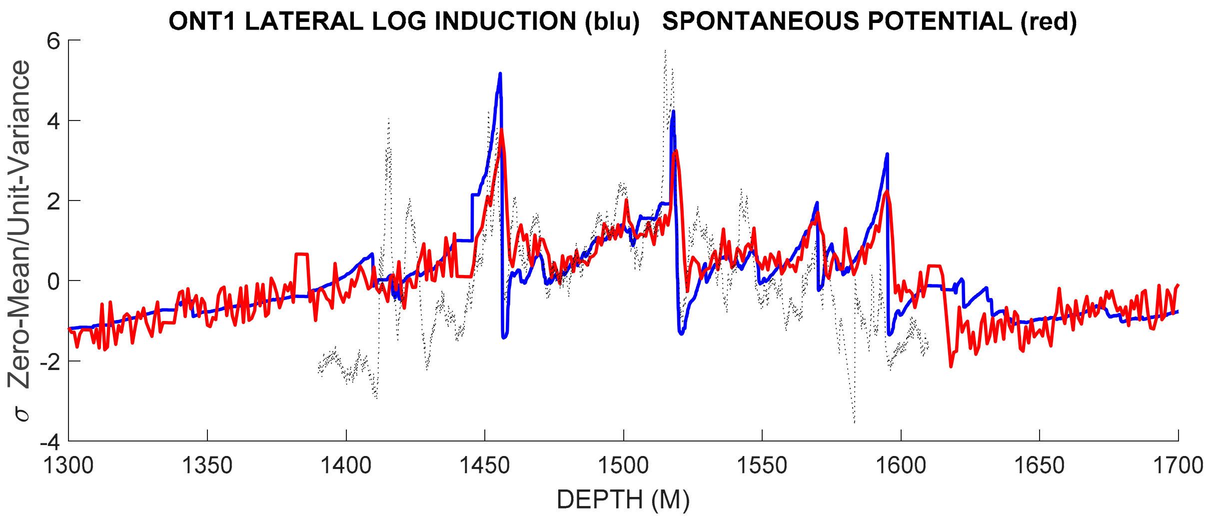

Preprints (www.preprints.org) | NOT PEER-REVIEWED | Posted: 18 September 2017 doi:10.20944/preprints201709.0079.v1

Peer-reviewed version available at Energies 2017, 10, 1979; doi:10.3390/en10121979

Figure 20. OTN1 galvanic property well-log data from granitic interval 1400m-1600m. Data are scaled to zero-mean/unit-variance format. Lateral log induction shown in blue; spontaneous potential shown in red; reference temperatures shown as black dots. The temperature data are shifted 10 meters due to depth discrepancy between separate well-log operations.

5.2. *Basement rock well-log and well-core empirics for KTB, Fennoscandia and Borrowdale metamorphic rock*

Compaction of spatially-uncorrelated porous media presents no conceptual difficulties. Upon increasing compaction, pore fluid driven out of a rock comprising spatially-uncorrelated grain populations leaves disordered grains squeezed together to fill pore voids with cements filling remaining interstices and no change in the degree of spatial organization [e.g., 33]. Less obvious is the effect of increased compaction on spatially-correlated porous media: what becomes of the spatial-correlation flow structures evident at 1-5km depths in reservoir rock worldwide when compaction reduces fluid content at sub-reservoir 5-10km depths? Are spatial correlation flow structure empirics (I)-(III) destroyed by continued compaction or are correlation structures preserved as relic or fossilised forms at increasing depth?

KTB well-log spatial fluctuation data at 6-8km depths indicate that crustal compaction processes preserve the spatial fluctuation heterogeneity and power-law spectral scaling, $S(k) \propto 1/k^{\beta}$, $\beta \sim 1$, observed at 1-5km depths (Figures 21-22; [24]). It is also seen that OTN1 and Outokumpu mining district Fennoscandia basement rock subject to past high-grade metamorphism preserves $S(k) \propto 1/k^{\beta}$, $\beta \sim 1$, spatial correlation spectral scaling to 2.5km depths (Figures 23-24; [28]).

Further, KTB well core from 4-5.5km depth (Figures 25-26; [24]) and well-flow data from highly metamorphosed low-porosity/low-permeability Borrowdale volcanics in Cumbria UK (Figures 27-29; [25-27]) preserve the spatial-correlation poroperm relation $\kappa(x,y,z) \propto \exp(\alpha\phi(x,y,z))$ to yield empirical values for poro-connectivity parameter α valid for low porosity basement rock. As porosity declines with increasing compaction, $\phi \rightarrow 0.01$, basement rock fluid flow continues to follow fracture-connectivity percolation flow paths characterized by increasing values of poro-connectivity parameter $\alpha \rightarrow$ 300-700.

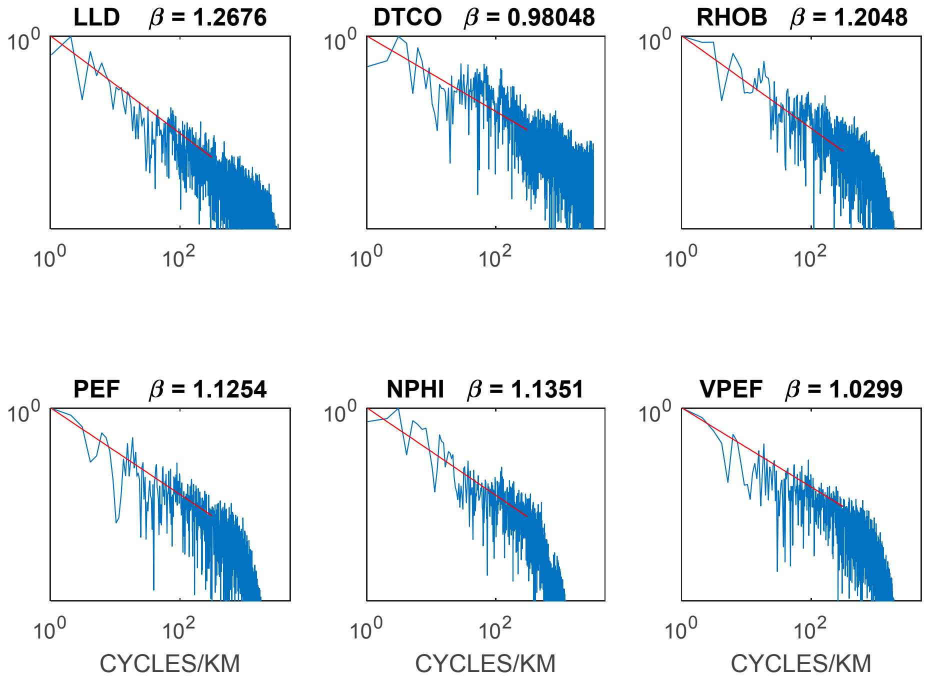

Figure 21. KTB well-log fluctuation power-spectral scaling inversely with spatial frequency, $S(k)\ 1/k^{\beta}$, $\beta \sim 1$; depth 6900-8130m; LLD=resistivity; DTCO=P-wave sonic; RHOB=mass density; PEF=photo-electric absorption; NPHI=neutron porosity; VPEF=volumetric photo-electric absorption [24].

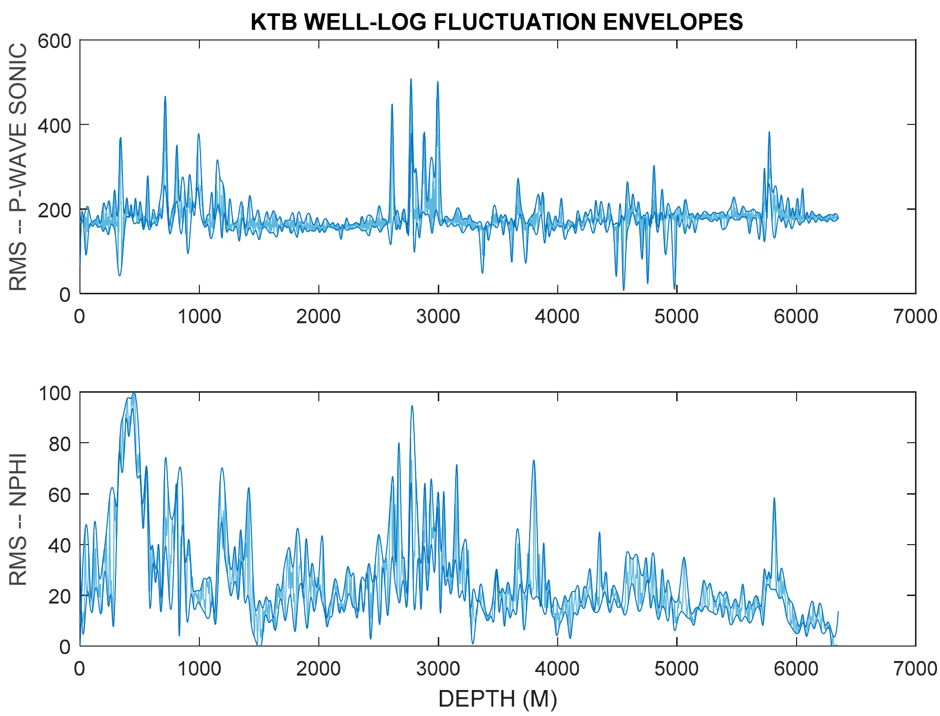

Figure 22. KTB well-log fluctuation amplitude preservation to 6.5km depth for P-wave sonic velocity (upper panel) and neutron porosity (lower panel) [24].

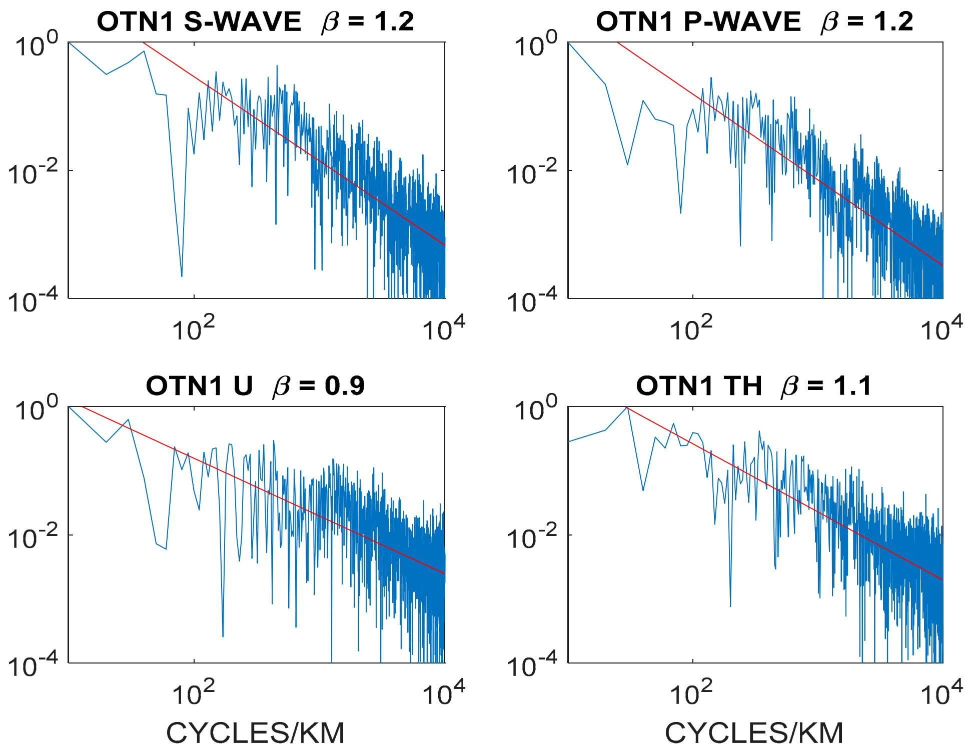

Figure 23. Sample OTN1 well-log spectral scaling S(k) ~ k^{β}, β ~ 1.2 ± 0.1; depth 1000m-1800m.

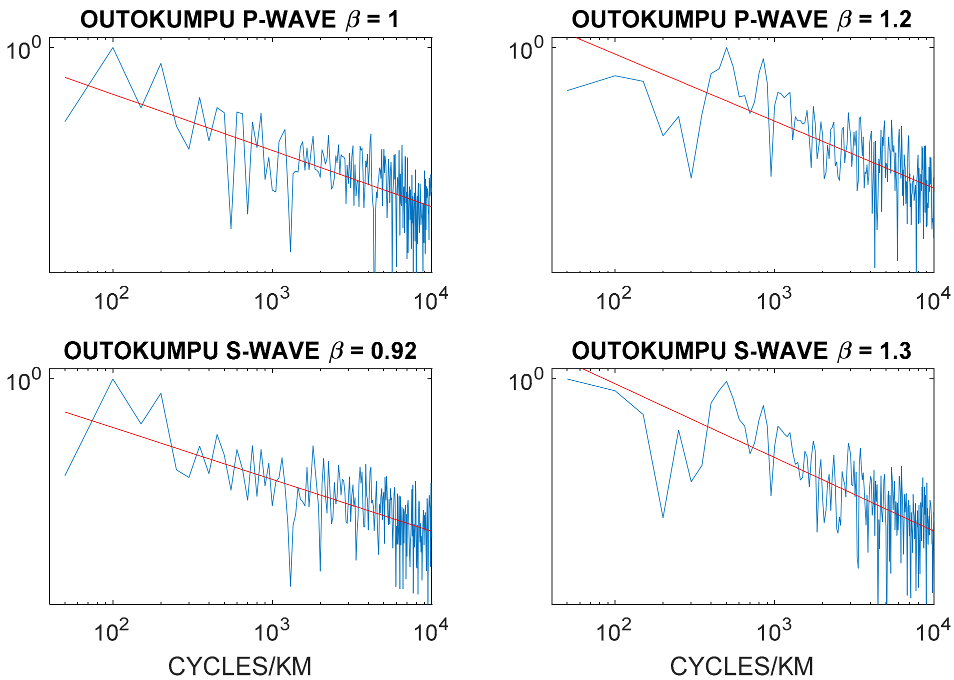

Figure 24. Sample Outokumpu well-log sonic-velocity spectral scaling S(k) ~ k^{β}, β ~ 1.2 ± 0; depths 950m-1500m and 1900m-2500m [28].

Preprints (www.preprints.org) | NOT PEER-REVIEWED | Posted: 18 September 2017 doi:10.20944/preprints201709.0079.v1

Peer-reviewed version available at *Energies* **2017**, *10*, 1979; doi:10.3390/en10121979

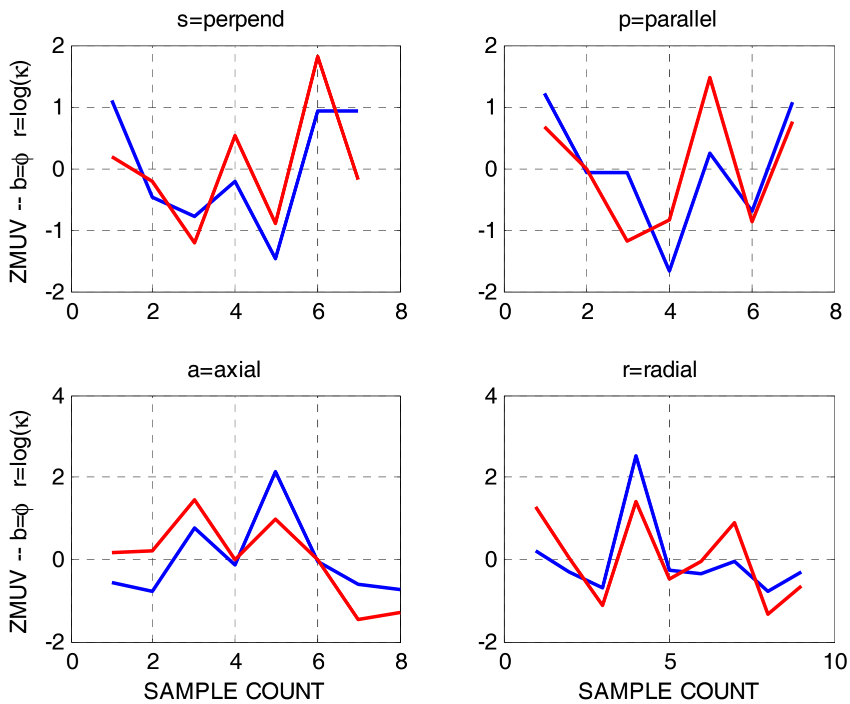

Figure 25. KTB well-core spatial correlation $\delta\phi \propto \delta\log(\kappa)$; zero-mean/univariance format; ϕ =blue, $\delta\log(\kappa)$ = red; well-core from depth interval 4000m-5500m [24].

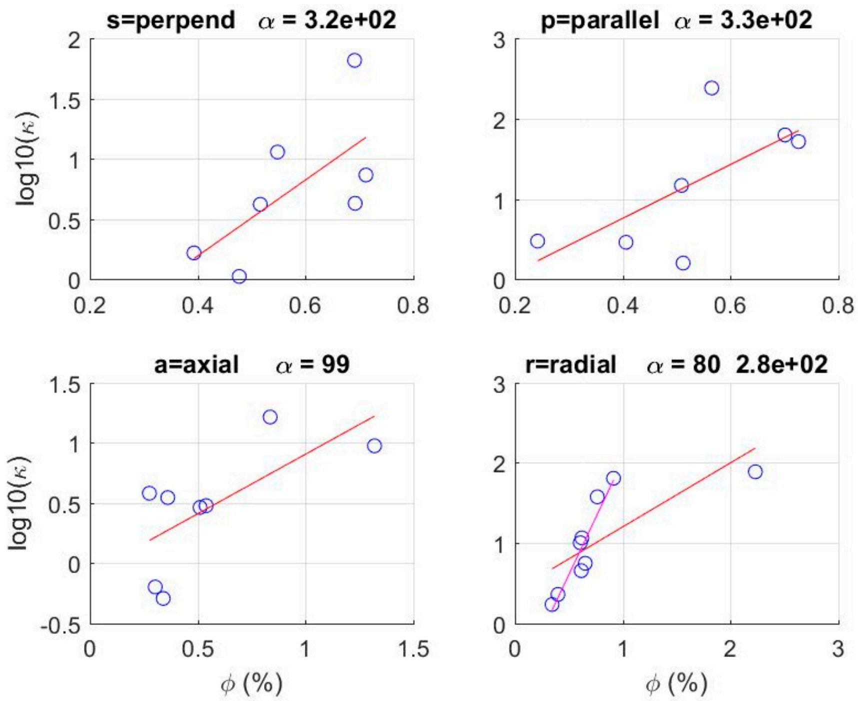

Figure 26. KTB well-core relation $\kappa \propto \exp(\alpha\phi)$; data blue circles; exponent fit for poro-connectivity parameter α (red); well-core from depth interval 4000m-5500m [24].

Peer-reviewed version available at Energies 2017, 10, 1979; doi:10.3390/en10121979

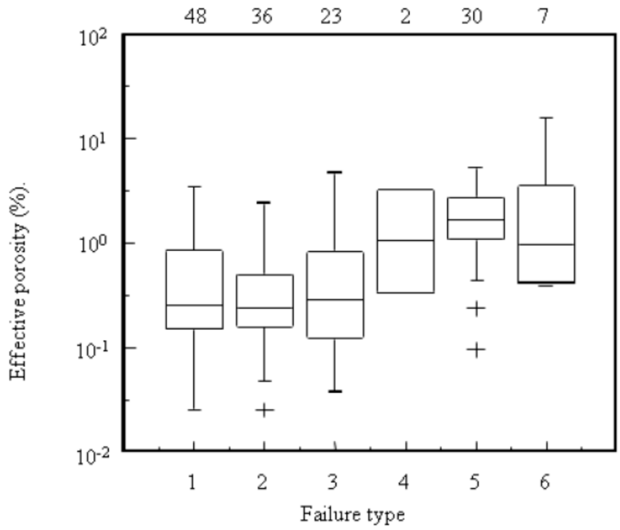

Figure 27. Well-core porosity, UK Nirex Borrowdale volcanics, Sellafield nuclear facility [27].

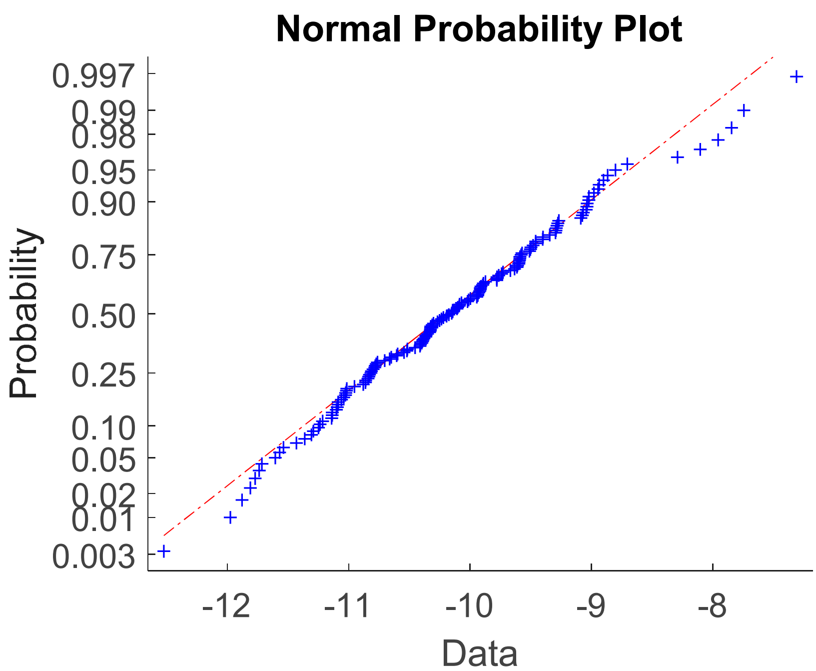

Figure 28. Synthetic data reproduction of field-scale wellbore hydrologic recharge distribution, UK Nirex Borrowdale Volcanics, Sellafield nuclear facility [25].

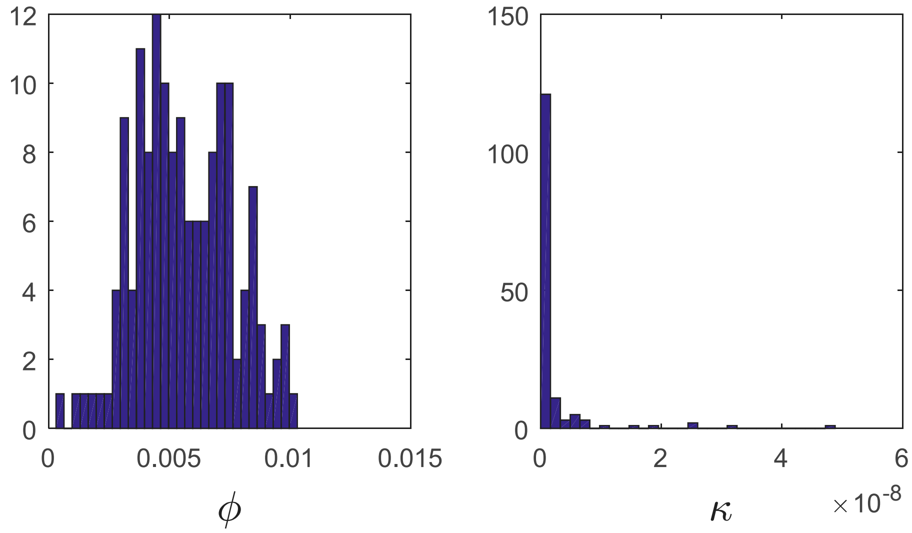

Figure 29. Porosity & permeability distributions for Figure 25 synthetic normal probability plot BVG wellbore recharge data. BVG field-scale permeability distribution minimum permeability $\kappa \sim 3\ 10^{-20}m^2$ for crustal volumes with no evidence of passing fluid through extent fracture structures versus minimum BVG permeability $\kappa \sim 3\ 10^{-18}m^2$ for crustal volumes with evidence of passing fluid through extent fracture structures.

5.3. Crustal deformation energetics for spatially-correlated crustal fluid flow granularity

Well-log, well-core, and well-productivity empirics focus on the granular rather than the spatially-averaged effective continuum nature of crustal rock. Key features of rock granularity emerge from considering the empirical spatial fluctuation relation between well-core porosity and well-core permeability, $\delta\phi \propto \delta\log(\kappa)$ [5-6,14-17].

Consider characterizing the porosity of a sample rock volume by a number n of grain-scale defects associated with the pore population. The grain-scale defects are cement bond failures that allow pores to communicate their fluid content with adjacent pores. Such defects are logically associated with pores as pores have the lowest elastic modulus and hence are subject to the greatest local strains within a crustal volume undergoing deformation during tectonic stress loading. In this granularity construct, grain-scale defect connectivity offers a simple quantitative account of crustal rock permeability associated with fluid percolation between pores.

For a sample rock volume with n defects, spatial connectivity between defects within the sample scales as the combinatorial factor $n! = n(n-1)(n-2)(n-3)\ldots\ldots1$. Permeability associated with defect connectivity is thus quantified as $\kappa \propto n!$. A well-known mathematical relation, $\log(n!) \sim n(\log(n)-1)$, quantifies the effect of incrementing the defect population of a sample volume by a small number $\delta n \ll n$. For porosity increment $n \rightarrow n + \delta n$, the incremented permeability is $\delta\log(n!) = \log((n+\delta n)!) - \delta\log(n!) \sim (n+\delta n)\log(n+\delta n) -1) - n(\log(n)-1)$, giving $\delta\log(n!) \sim \delta n \log(n)$. This relation exactly expresses the empirical property of well-core poroperm sequences, $\delta\phi \propto \delta\log(\kappa)$. For porosity proportional to defect number, $\phi \propto n$, and permeability proportional to defect connectivity factor $n!$, $\kappa \propto n!$, cement bond defect connectivity in a granular medium gives a direct mechanism for the essentially universally observed properties of well-core poroperm spatial correlation (II) and its associated lognormality of crustal permeability distributions at core scale and well-production at field scale (III).

Placing EGS-type stimulation in wellbore-centric fluid pressurization context, the above granularity construct quantifies the effect on inter-granular fluid flow of introducing a single grain-scale defect into a poroperm structure, $n \rightarrow n+1$. The incremental effect differs for Poiseuille flow versus granular percolation: adding a single defect to a conduit between continuum dislocation surfaces has a smaller effect than adding a single defect to disseminated/granular-connectivity structures of empirics (I)-(III).

For a fluid of dynamic viscosity μ driven by pressure gradient P', Poiseuille volumetric flow per unit breadth of the flow front is Q [m^2/s] = $P' \Delta^3/12\mu$ [Pa/m m^3/Pa·s]. The corresponding fluid velocity is v [m/s] = $P' \Delta^2/12\mu$. For a gap Δ comprising a number n defects in the continuum flow structure, the mean gap increment is $\delta\Delta \sim \Delta/n$. It follows from $(v + \delta v)/v = 1 + \delta v/v = (\Delta + \delta\Delta)^2/\Delta^2 \sim 1 + 2\delta\Delta/\Delta$, that adding a single defect to the medium increases the gap by Δδ and increases fluid velocity by $\delta v/v \sim 2/n$.

For the disseminated empirical granular medium with fluid velocity $v \propto \exp(\alpha\phi)$, the equivalent increment gives $(\kappa + \delta\kappa)/\kappa = 1 + \delta\kappa/\kappa \propto \exp(\alpha\delta\phi) \sim 1 + \alpha\delta\phi$, whence for $\phi = n\delta\phi$, $\delta\kappa/\kappa = \delta v/v \sim \alpha\delta\phi = \alpha\phi/n$. For standard reservoir formations with porosity in the range $.1 < \phi < .3$, the empirical values of α, $20 < \alpha < 40$, give $\alpha\phi \sim 6 \pm 2$ fluid velocity increment factor for aquifer formations. For basement rock with porosity an order of magnitude smaller, $\phi \sim .01$, the value of α increases by an order of magnitude, $300 < \alpha < 700$, giving an empirical estimate of fluid velocity increment factor $\alpha\phi \sim 5$ for basement formations.

Allowing for rough surfaces at large confining stresses in the deep crust, the effective exponent characteristic of Poiseuille flow mechanics significantly increases [34]. If fracture surface roughness is included within the flow conduit, exponents for the effective Poiseuille flow factor Δ^m are modelled to increase from 3 to ~ 5-10 [35-36]. The increased exponent heightens the effect of increments in defect population on fluid flow in tight rock.

Table 1. The relative effect of incremental permeability increases for smooth and rough Poiseuille flow and for granularity percolation flow for empirics (I)-(III) [34-36].

Flow Geometry	Flow Law	Flow Velocity	Velocity Increment	Increment Factor
Smooth Continuum	$Q = P' \Delta^3/12\mu$	$v \propto \Delta^2$	$\delta v/v \sim 2/n$	2
Granular	$v = \kappa/\mu\ P'$	$v \propto \exp(\alpha\phi)$	$\delta v/v \sim \alpha\phi/n$	~ 5
Rough Continuum	$Q = P' \Delta^m/12\mu$	$v \propto \Delta^{m-1}$, $m \sim$ 5-10	$\delta v/v \sim (m-1)/n$	~ 4-9

For wellbore-fluid stimulation of crustal permeability, Table 1 indicates that creating a grain-scale defect in a crustal volume produces greater flow effect if the defect is embedded in a granular percolation flow structure than if the defect contributes to a conduit gap in the smooth continuum flow structures of the discrete fracture concept of EGS stimulation. It follows that energy expended by wellbore pressurization is more effective in dissipating wellbore fluid pressure fronts if defects generated by fluid pressures contribute to granularity flow structures than if they contribute to continuum flow structures. If the observed effect of large confining stresses is taken into account, the empirical granularity picture is consistent with rough fracture surfaces expected at the limit of thin flow conduit gaps.

Given the extensive evidence of well-log, well-core, and well-flow empirics (I)-(III) as the ambient condition of crustal rock, we may argue that wellbores penetrating crustal media will typically encounter localised disseminated/granularity rather than planar geometric/continuum flow surfaces associated with discrete fracture displacement structures.

We can interpret Table 1 further to argue that the ambient crustal empirics (I)-(III) result from the implied energetics of defect insertion through rock-fluid interaction. Rock stress involving fluids is more easily dissipated if fluid permeability stimulation proceeds through spatially-correlated fracture-connectivity granularity rather than through spatially-uncorrelated effective-medium planar continuum displacements. For generating ambient crustal fluid-rock flow conditions, the fact that porosity increments require doing work against confining stresses means that it is energetically favourable for defect enhancement to proceed in a spatially-correlated granularity medium than in a spatially-uncorrelated continuum medium. Discrete fracture systems may thus be seen to characterize crustal tectonic settings in which solid-rock displacement rates due to far-field tectonic plate motion exceed the rate at which fluid pressures can dissipate through slower fracture-connectivity mechanisms. EGS mechanisms based on local wellbore-centric fluid pressurization rather than elastic stress generated by far-field tectonics may thus couple more readily to the slower ambient-crust defect injection processes leading to spatially-correlated granularity than to the faster defect injection processes leading to discrete-fracture displacements.

5.4. EGS couplet scale dimensions

The irreducible statement of EGS principle is to pass fluid from an injector wellbore through an ambient hot crustal volume to a producer wellbore at a sufficient rate over a sufficient length of time that the recovered heat energy covers the cost of (i) drilling sufficiently deep wells to access sufficient temperature and (ii) stimulating the wellbore-centric crustal volumes to sufficient radius to access a sufficient crustal volume.

The scale-sufficiency conditions for an EGS wellbore-centric flow doublet are simply quantified by considering the radial transfer of heat energy via wellbore fluid injected into the surrounding crust. For wellbore radius r_0 and length ℓ in a crustal volume of porosity ϕ, fluid of temperature T_0 and volumetric heat capacity ϱC injected or produced at radial velocity v_0 steadily transfers $Q = 2\pi r_0 \phi v_0 \ell \varrho C T_0$ watts of heat energy from/to the wellbore to/from the crust. The crustal temperature surrounding an injector wellbore grows as a function of radius and time from the initial crustal temperature as,

$$T(r,t) = 2/\pi\ T_0(r/r_0)^{\nu} \int dk/k \quad \exp(-Dk^2t)\ [J_\nu(kr)Y_\nu(kr_0) - Y_\nu(kr)J_\nu(kr_0)]/[J_\nu^2(kr_0) + Y_\nu^2(kr_0)], \qquad (11)$$

for $D \equiv K/\varrho C$ the thermal diffusivity of the crustal medium, $\nu = P_e/2$ one-half the Peclet number $P_e \equiv r_0\phi v_0/D$, and $J_\nu(:)$ and $Y_\nu(:)$ the order ν Bessel functions of the first and second kind respectively [37].

Peclet number $P_e = r_0\phi v_0/D = r_0\phi v_0\varrho C/K$ links the crustal temperature growth to the rate at which the wellbore supplies heat,

$$P_e = Q/2\pi K\ell T_0. \qquad (12)$$

For a given injection of heat energy Q, the system Peclet number of resultant temperature field diminishes in proportion to the wellbore length ℓ and fluid temperature T_0. For a maximally stimulated wellbore that supports $P_e \sim 5$ heat transport across every meter of wellbore length for crustal rock temperature 100°C, the total wellbore-centric heat extraction rate is Q ~ 10MW per km of wellbore.

Figure 30 shows the temperature growth curve $T(r,t)$ as a function of Peclet number. A km-long EGS wellbore doublet capable of producing Q ~ 10MW heat energy for 30 years from crust at 100°C requires a wellbore doublet radially offset by a distance ~ 50 meters. An EGS wellbore doublet separated by 50 meters thus requires that each wellbore be effectively stimulated to a 25m radius.

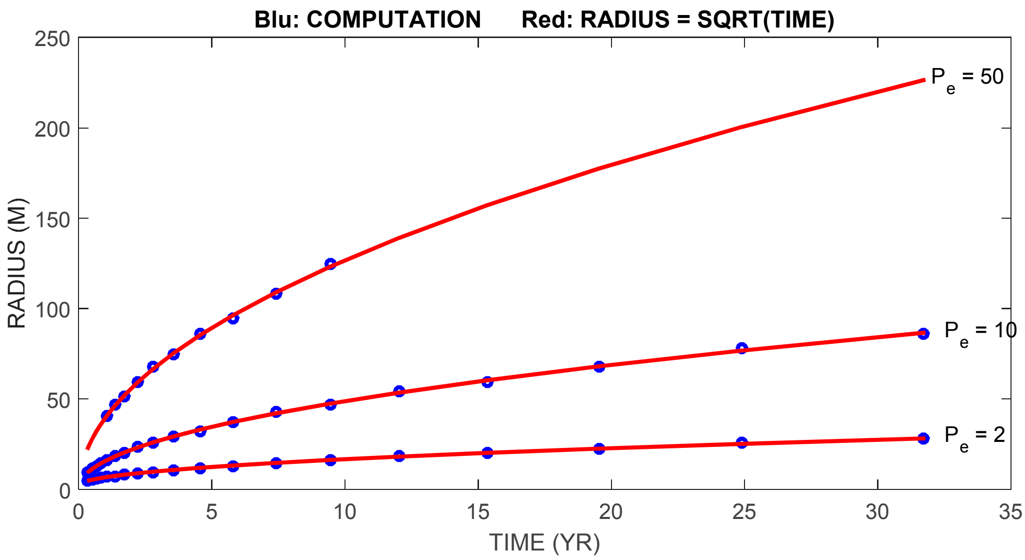

Figure 30. For Peclet number $P_e = r_0\phi v_0/D$ applied to a wellbore-centric heat exchange flow system, an EGS wellbore couplet requires a crustal volume of order given by the length of the wellbores and by the radial offset of the wellbore couplet (vertical axis) for heat supply over a given period of time (horizontal axis).

Peer-reviewed version available at Energies 2017, 10, 1979; doi:10.3390/en10121979

5. Summary/Conclusions

Despite abundant well-log, well-core, and well-flow counter-evidence, the working assumption that fluid flow in geological formations is effectively uniform due to spatial averaging over uncorrelated poroperm fluctuations has remained in place since the mid-19th century observations and innovations of Darcy and Dupuit [39-48]. This stasis is essentially a practical matter: for both groundwater and hydrocarbon crustal fluids, it has been found cost effective to ignore manifest fluid flow heterogeneity by the simple practice of drilling more wells.

Groundwater wells are shallow and therefore inexpensive. The considerable value of hydrocarbon fluids means that, first, a relatively few high-flow/high-profit oil/gas wells tend to cover the cost of many low-flow oil/gas wells, and, second, the population of many low-flow wells that accompany the few high-flow wells are generally profitable for considerable lengths of time [19].

Geothermal energy provision, in contrast, lacks the well-cost offsets afforded groundwater and hydrocarbon reservoir fluids. In natural convective geothermal systems with high fluid temperatures and permeabilities, the excessively large flow-rate demand to power turbines means that crustal flow heterogeneity cannot be cost-effectively solved by the rubric of spatial averaging [21]. Subsurface imaging is required to achieve 'smart-drilling' practice to keep well costs down in tapping naturally convective geothermal flow systems [18]. In low-porosity/low-permeability basement rock geothermal systems, the high cost of drilling and the limited technical means of EGS permeability enhancement for wellbore-to-wellbore flow mean that net fluid through-put remains generally non-commercial for power-production [1-2].

Balancing the negatives of basement rock EGS geothermal heat energy provision are the positives of great abundance of carbon-free heat energy for direct use purposes. The accessible heat energy in a 50m thick crustal section 5km below any of Finland's district heating plants with a 5-km municipal service radius is of the order $E = \pi R^2 \ell\, \varrho C\, T \sim 0.75 \cdot 10^{18}$ GJ ~ 150 million BOE, the energy content of a sizeable conventional oil field [48]. The heat energy content accessible to a single fully-stimulated $P_e \sim 5$ EGS doublet of 50m offset and 3 km horizontal extent to produce 30MW heat energy extraction is ~ 1000 times the annual energy consumption of currently operating district heating plants. From Figure 30, conductive recharge of an EGS 30MW doublet heat extraction crustal volume can supply heat to the injector-producer wellbore pair for ~ 30 years.

Our OTN1 wellbore temperature event modeling calibration of naturally occurring basement rock fracture-connectivity flow systems suggests that the necessary condition of 'full stimulation' for EGS wellbore doublets is that every 3-5m interval of wellbore supports a $P_e \sim 5$-10 fracture-connectivity flow path between the doublet pair. Model estimates of natural flow stimulation through naturally enhanced poro-connectivity parameter α indicates that doubling the poro-connectivity from ambient crust value $\alpha \sim 500$ derived from well-core data (e.g., Figures 25-29, [24-27]) to $\alpha \sim 1000$ achieves the necessary stimulation goal for wellbore-centric flow systems of order 10-meter radius.

Preprints (www.preprints.org) | NOT PEER-REVIEWED | Posted: 18 September 2017 doi:10.20944/preprints201709.0079.v1

Peer-reviewed version available at Energies 2017, 10, 1979; doi:10.3390/en10121979

Cross-well fracture-connectivity paths may be a narrow P_e ~ 10-15 flow structure or broader P_e ~ 5 flow structures, but radial cross-well fluid flow must occur along the entire length ℓ of the injection-production wellbore pair to achieve full EGS heat production. In this definition of fully-stimulated EGS wellbore production Q, we must write a cautionary $Q = 2\pi P_e K \ell' T_0$ where the effective length unit of wellbore heat production is 3m, so that $\ell' = \ell/3$. Additionally, to produce ~ 10MW from fully-stimulated wellbore-pairs for 30 years, the radial cross-well flow-connectivity flow structures must be of order 50m path length, equating to ~ 25m stimulation radius for each wellbore. Development of the full axial-stimulation and the 25m radial-stimulation conditions indicated by OTN1 temperature event calibrations for deep crustal basement EGS are currently very much works in progress.

Acknowledgements The research presented in this paper is wholly was funded by St1 Deep Heat Ltd, Purotie 1, 00381 Helsinki, Finland. Publication costs are likewise supported by St1 Deep Heat Ltd.

Conflicts of Interest The authors declare that there are no conflicts of interest regarding the publication of this paper.

Author Contributions The St1 Deep Heat Ltd OTN1 pilot well drilling, coring and logging project was planned and executed under the supervision of Tero Saarno. Ilmo Kukkonen was custodian and evaluator of OTN1 well-log and well-core data. Peter Leary and Peter Malin provide the continuing St1 Deep Heat Ltd drilling and crustal stimulation project OTN2 and OTN3 deep wells with seismic monitoring capability and well-log data interpretations. Peter Leary performed the computations and wrote the text.

Appendix A. 2D steady-state wellbore-centric heat transport analytics

In the approximation that Darcy fluid flow velocity can be approximated as $v(r) \sim r_0 v_0/r$ in a wellbore-centric radial domain $r_0 \le r \le r_1$, the conservation of heat energy condition

$$\nabla^2 T(r) = 1/D\, \phi \mathbf{v}(r)\cdot\nabla T(r), \qquad \text{(A1)}$$

can be expressed analytically. For radial component divergence operator $\nabla\cdot\mathbf{A}(r) = 1/r\, \partial_r(rA_r)$, (A1) becomes

$$\partial_r^2 T(r) + (1 - P_e)/r\, \partial_r T(r) = 0, \qquad \text{(A2)}$$

for $P_e = r_0 \phi v_0/D$, from which it follows that

$$T(r) = T_0 + (T_1 - T_0)\,((r/r_0)^{P_e} - 1)\,/\,((r_1/r_0)^{P_e} - 1). \qquad \text{(A3)}$$

The wellbore-centric steady-state heat advection expression (A3) closely parallels the Bredehoeft & Papadopulos [29] expression for steady-state heat advective transport in a plane-layered medium,

$$T(z) = T_0 + (T_L - T_0)\cdot(e^{\beta z/L} - 1)/(e^{\beta} - 1), \qquad \text{(A4)}$$

with Peclet number given as $\beta \equiv v_0 \varrho C L/K$ for a layer of thickness L with thermal constants $\varrho C/K = 1/D$ traversed by a fluid front moving at velocity v_0.

The role of crustal porosity ϕ in weighting the fluid heat transport is omitted from the derivation of (A3), doubtless in consequence of there being little observational control over fluid flow through large-scale sequences of crustal layering and the likelihood that many such layers have moderate to high porosity. As neither of these factors come into play for wellbore-centric flow in basement rock, we carry porosity as an explicit factor for characterizing heat transport.

Wellbore-centric radial temperature distributions (A3) are shown in Fig A1 for a sequence of Peclet numbers $0 < P_e < 10$. The red curve denotes pure conduction. The central straight-line blue curve denotes $P_e = 1$, for which thermal conduction transport equal fluid advective transport. Blue curves to the left of the $P_e = 1$ curve have $P_e < 1$ while blue curves to right of the $P_e = 1$ curve have $1 < P_e < 10$.

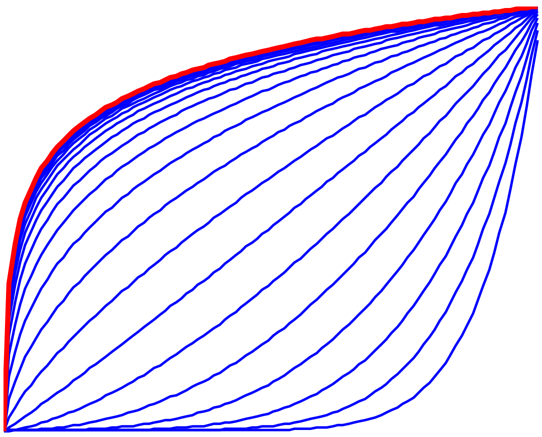

Figure A1. Steady-state wellbore-centric radial temperature profiles $T(r) = T_0 + (T_1 - T_0)((r/r_0)^{Pe} - 1)/((r_1/r_0)^{Pe} - 1)$ for range of fluid flow velocities associated with Peclet numbers $P_e = r_0 \phi v_0/D$. Fluid fow is in a cylindrical section with radius r_1 at fixed temperature T_1 and a central wellbore of radius r_0 at temperature T_0. Fluid advection velocity fields are determined by fluid velocity v_0 at the central wellbore, $v(r) \sim r_0 v_0/r$. The amount of heat carried by the fluid is proportional to the porosity ϕ of the flow medium.

It is seen in Figure A1 that for $P_e > \sim 3$, the radial thermal gradient vanishes near the wellbore. For $P_e > \sim 3$ all heat transport near the wellbore is by advective flow. We can thus expect observed wellbore temperature fluctuations to correspond to $P_e > \sim 3$ fluid advection along the radial fracture-connectivity pathway. The numerical model result shown in Figure 9 indicates that the finite element solution to conservation of thermal energy constraint (2) conforms to the 2D analytic solution (A3) for spatially-averaged radial flow in a wellbore-centric geometry.

The spherical analogue temperature field $T_0 \le T(r) \le T_1$ for radial shells centered on a central source/sink cavity is

Preprints (www.preprints.org) | NOT PEER-REVIEWED | Posted: 18 September 2017 doi:10.20944/preprints201709.0079.v1

Peer-reviewed version available at Energies 2017, 10, 1979; doi:10.3390/en10121979

$$T(r) = T_0 + (T_1 - T_0)\,(exp(P_e(r_0/r - 1)) - 1) / (exp(P_e(r_0/r_1 - 1)) - 1) \text{ (sphere).} \quad \text{(A5)}$$

From (A3) and (A5), the associated Darcy radial flow velocity fields are

$$v(r) = v_0r_0/r, \text{ (cylinder)}$$

$$v(r) = v_0r_0^2/r^2, \text{ (sphere)}$$

and advected heat $Q(r) = K\partial_r T(r) - \varrho C v(r) T(r)$ has the form of thermal conduction with heat flux magnitude $Q_0 = v_0\varrho C(T_1 - T_0)$,

$$Q(r) = Q_0\, r_0/r, \text{ (cylinder)}$$

$$Q(r) = Q_0\, r_0^2/r^2, \text{ (sphere).}$$

In the absence of fluid flow, $v(r) = 0$, advective heat flow reduces to thermal conductive heat flow condition $\nabla^2 T(r) = 0$ in the radial domain $r_0 \le r \le r_1$,

$$T(r) = T_0 + (T_1 - T_0)/ln(r_0/r_1)\cdot ln(r_0/r),\ Q(r) = Q_0r_0/r, \quad \text{(cylinder)}$$
$$T(r) = T_0 + (T_1 - T_0)/(r_0/r_1 - 1)\cdot(r_0/r - 1),\ Q(r) = Q_0r_0^2/r^2 \text{ (sphere)}$$

where Q_0 is the flux at the inner radius r_0, $Q_0 = K(T_1 - T_0)/r_0/ln(r_0/r_1) < 0$ for cylindrical flow and $Q_0 = K(T_1 - T_0)/r_0^2/(1/r_1 - 1/r_0) < 0$; the negative signs for the heat flow magnitudes indicate inward heat flow.

In the limit of zero Darcy flow velocity, advection forms of heat transport (A3) and (A5) reduce to the above conduction forms. For (A3), expressing exponential function e^x as the limit of $(1 + x/n)^n$ as $n \to \infty$ gives the limiting case $\alpha \to 0$ for the ratio $(x^\alpha - 1)/(x_0^\alpha - 1)$ as

$$(x^\alpha - 1)/(x_0^\alpha - 1) = (e^{\alpha lnx} - 1)/(e^{\alpha lnx_0} - 1) \sim ((1 + \alpha lnx/n)^n - 1)/((1 + \alpha lnx_0/n)^n - 1)$$

$$\sim (1 + \alpha lnx - 1)/(1 + \alpha lnx_0 - 1) = ln(1/x)/ln(1/x_0).$$

For (A5) in the limit $P_e \to 0$, $(exp(P_e(r_0/r - 1)) - 1)/(exp(P_e(r_0/r_1 - 1)) - 1) \sim (1 + P_e(r_0/r - 1) - 1)/(1 + P_e(r_0/r_1 - 1) - 1) = (r_0/r - 1)/(r_0/r_1 - 1)$.

When the inner radius r_0 becomes effectively very large, $r_0 \to \infty$, the above expressions revert to the plane flow geometry case for $P_e/r_0 = v_0/D = v_0\varrho C/K$ and $\beta \equiv v_0\varrho CL/K$,

$$T(r_0 + \delta r) \propto (1 + \delta r/r_0)^\alpha = (1 + \delta r/r_0)^{v0r0/D} \sim exp(v0\delta r/D) = exp(\beta\delta r/L) \quad \text{(cylinder)}$$

$$v(r_0 + \delta r) = v_0/(1 + \delta r/r_0) \sim v_0,$$

$$Q(r_0 + \delta r) = Q_0/(1 + \delta r/r_0) \sim Q_0 \equiv v_0\varrho C(T_1 - T_0),$$

$$T(r_0 + \delta r) \propto exp(\alpha\delta r/r_0) = exp(\delta r v_0\varrho C/K) = exp(\beta\delta r/L) \quad \text{(sphere)}$$

$$v(r_0 + \delta r) = v_0/(1 + 2\delta r/r_0) \sim v_0,$$

$$Q(r_0 + \delta r) = Q_0/(1 + 2\delta r/r_0) \sim Q_0 \equiv v_0\varrho C(T_1 - T_0).$$

References

1. Moeck IS. Catalog of geothermal play types based on geologic controls, *Renewable and Sustainable Energy Reviews*, **2014**, *37*, 867–882.
2. Moeck IS; Beardsmore G. A new 'geothermal play type' catalog: Streamlining exploration decision making, *39th Workshop Geothermal Reservoir Engineering*, **2014**, Stanford University, February 24-26, SGP-TR-202.
3. Bendall B; Hogarth R; Holl H; McMahon A; Larking A; Reid P. Australian Experiences in EGS Permeability Enhancement – A Review of 3 Case Studies, *39th Workshop Geothermal Reservoir Engineering*, **2014**, Stanford University, February 24-26, SGP-TR-202.
4. Bertani R. Geothermal Power Generation in the World 2010-2014 Update Report, WGC2015, **2015**, 19-24 April, Melbourne AU.
5. Leary P; Malin P; Niemi R. Finite-Element Modelling of Wellbore-Observed Fracture-Borne Heat Advection – Application to EGS Stimulation in Basement Rock, *41st Workshop Geothermal Reservoir Engineering*, **2017a**, Stanford University, February 13-15, SGP-TR-212.
6. Leary P; Malin P; Niemi R. Fluid Flow & Heat Transport Computation for Power-law Scaling Poroperm Media, *Geofluids*, **2017b**, (in press).
7. Barton CA; Zoback MD; Moos D. Fluid flow along potentially active faults in crystalline rock, *Geology*, **1995**, *23*, 683-686; doi: 10.1130/0091-7613.
8. Ito T; Zoback MD. Fracture permeability and in situ stress to 7 km depth in the KTB scientific drillhole, *Geophysical Research Letters*, **2000**, *27*, 1045-1048.
9. Leary PC. Deep borehole log evidence for fractal distribution of fractures in crystalline rock, *Geophysical Journal International*, **1991**, *107*, 615-628.
10. Bean CJ. On the cause of 1/f power spectral scaling in borehole logs, *Geophysical Research Letters*, **1996**, *23*, 32119-3122.
11. Leary PC. Rock as a critical-point system and the inherent implausibility of reliable earthquake prediction, *Geophysical Journal International*, **1997**, *131*, 451-466.
12. Dolan S; Bean CJ; Riollet B. The broad-band fractal nature of heterogeneity in the upper crust from petrophysical logs, *Geophysical Journal International*, **1998**, *132*, 489-507.
13. Leary PC. Fractures and physical heterogeneity in crustal rock, in *Heterogeneity of the Crust and Upper Mantle – Nature, Scaling and Seismic Properties*, JA Goff & K Holliger eds., Kluwer Academic/Plenum Publishers, New York, **2002**, 155-186.
14. Leary PC; Al-Kindy F. Power-law scaling of spatially correlated porosity and log(permeability) sequences from northcentral North Sea Brae oilfield well core, *Geophysical Journal International*, **2002**, *148*, 426-442.
15. Leary PC; Walter LA. Crosswell seismic applications to highly heterogeneous tight gas reservoirs, *First Break*, **2012**, *26(3)*, 49-55.
16. Leary PC; Malin PE; Pogacnik JA. Computational EGS -- Heat transport in 1/f-noise fractured media, *37th Workshop Geothermal Reservoir Engineering*, **2012**, Stanford University, January 30 - February 1, SGP-TR-194

17. Pogacnik J; Leary P; Malin P; Geiser P; Rugis J; Valles B. Flow Lognormality and Spatial Correlation in Crustal Reservoirs: III – Natural Permeability Enhancement via Biot Fluid-Rock Coupling at All Scales, WGC2015, **2015**, 19-24 April, Melbourne AU.
18. Malin P; Leary P; Shalev E; Rugis J; Valles B; Boese C; Andrews J; Geiser P. Flow Lognormality and Spatial Correlation in Crustal Reservoirs: II – Where-to-Drill Guidance via Acoustic/Seismic Imaging, WGC2015, **2015**, 19-24 April, Melbourne AU.
19. US Energy Information Administration. *Distribution and Production of Oil and Gas Wells by State*, **2011**, www.eia.gov/pub/oil_gas/petrosystem/all-years-states.xls.
20. IEA. *Special Report: Golden Rules for Golden Age of Gas*, International Energy Agency, **2012**, www.iea.org; http://www.iea.org/publications/freepublications/publication/WEO2012_GoldenRulesReport.pdf, 150p.
21. IFC. *Success of Geothermal Wells: A global study*, International Finance Corporation, Washington DC, **2013**, 80pp.
22. Gustafson G. Strategies for groundwater prospecting in hard rocks: a probabilistic approach, *Norgesqeoloqiske undersøkelse Bulletin*, **2002**, 439, 21-25.
23. Banks D; Gundersen P; Gustafson G; Mäkelä J; Morland G. Regional similarities in the distributions of well yield from crystalline rocks in Fennoscandia, *Norges geologiske undersøkelse Bulletin*, **2010**, 450, 33–47.
24. KTB http://www-icdp.icdp-online.org/sites/ktb/welcome.html.
25. Chaplow R. The geology & hydrology of Sellafield: an overview, *Quarterly Journal of Engineering Geology*, **1996**, *29*, S1-12; doi: 10.1144/GSL.QJEGH.1996.029.S1.01.
26. Sutton JS. Hydrogeological testing in the Sellafield area, *Quarterly Journal of Engineering Geology*, **1996**, *29*, S29-38; doi: 10.1144/GSL.QJEGH.1996.029.S1.03.
27. Entwisle DC; Hobbs PRN; Jones LD; Gunn D; Raines MG. The relationships between effective porosity, uniaxial compressive strength and sonic velocity of intact Borrowdale Volcanic Group core samples from Sellafield, GEGE2166-RAD, **2003**, nora.nerc.ac.uk/504073/1/NIREX_paper_2003%20(2).pdf.
28. Kukkonen IT. Outokumpu Deep Drilling Project 2003–2010, *Geological Survey of Finland Special Paper 51*, **2011**, pp252.
29. Bredehoeft JD; Papaopulos IS. Rates of vertical groundwater movement estimated from the Earth's thermal profile, *Water Resources Research*, **1965**, *1*, 325–328; doi: 10.1029/WR001i002p00325.
30. Hughes TJR. *The Finite Element Method*, Prentice-Hall, New Jersey 07632, **1987**, pp797; ISBN 0-13-317025-X.
31. Hjelmstad KD. *Fundamentals of Structural Mechanics*, Springer, New York, **2005**, pp480.
32. *Partial Differential Equation Toolbox User's Guide R2015b*, MathWorks, 3 Apple Hill Drive, Natick MA 01760-2098, **2015**.
33. Nordahl K; Ringrose P. Identifying the representative elementary volume for permeability in heterolithic deposits using numerical rock models, *Mathematical Geosciences*, **2008**, *40*, 753–771.
34. Witherspoon PA; Wang JSY; Iwail K; Gale JE. Validity of cubic law fluid flow in a deformable rock fracture, *Water Resources Research*, **1980**, *16*, 1016-1024.
35. Sisavath S; Al-Yaarubi A; Pain CC; Zimmerman RW. A simple model for deviations from the cubic law for a fracture undergoing dilation or closure, *PAGEOPH*, **2003**, *160*, 1009–1022.

36. Zimmerman RW. The history and role of the cubic law for fluid flow in fractured rocks, Session H071 Dynamics of fluids and transport in fractured porous media, American Geophysical Union, San Francisco, 3-7 December 2012.
37. Carslaw HS; Jaeger JC. *Conduction of Heat in Solids*, Clarendon Press, Oxford, **1959**, pp510.
38. Darcy H. *Les Fontaines publiques de la ville de Dijon*, Victor Dalmont, **1856**, Paris.
39. Dupuit J. *Etudes Theoriques et Pratiques sur le Mouvement des Eaux dans les Canaux Decouverts et a Travers les Terrains Permeables*, **1863**, 2nd ed., Dunod, Paris.
40. Theis CV. The relation between the lowering of the piezometric surface and the rate and duration of discharge of a well using ground-water storage, *Transactions of the American Geophysical Union*, **1935**, Part 2, 519-524, August 1935; DOI: 10.1029/TR016i002p00519.
41. Muskat M. The Flow of Homogeneous Fluids Through Porous Media, McGraw-Hill, **1937**, pp763.
42. Hubbert MK. Motion of ground water, *Transactions of the New York Academy of Sciences*, **1941**, *Series II No 3*, 39-55.
43. Hubbert MK. Darcy's law and the field equations of the flow of underground fluids, *International Association of Scientific Hydrology, Bulletin*, **1957**, *2:1*, 23-59; doi: 10.1080/02626665709493062.
44. Bear J. *Dynamics of fluids in porous media*, American Elsevier, **1972**, New York.
45. Koltermann CE; Gorelick SM. Heterogeneity in sedimentary deposits: A review of structure-imitating, process-imitating, and descriptive approaches, *Water Resources Research*, **1996**, *32*, 2617-2658.
46. Ingebritsen S; Sanford W; Neuzil C. *Groundwater in Geological Processes*, **2006**, Cambridge University Press, pp536.
47. Sanyal SK; Butler SJ. Geothermal Power Capacity from Petroleum Wells – Some Case Histories of Assessment, World Geothermal Congress 2010, Bali, Indonesia, 25-29 April **2010**.
48. Drew LJ; Attanasi E; Schuenemeyer JH. Observed Oil and Gas Field Size Distributions: A Consequence of the Discovery Process and Prices of Oil and Gas, *Mathematical Geology*, **1988**, *20*, 939-953.

1. Author 1, A.B.; Author 2, C.D. Title of the article. *Abbreviated Journal Name* **Year**, *Volume*, page range, DOI.
2. Author 1, A.; Author 2, B. Title of the chapter. In *Book Title*, 2nd ed.; Editor 1, A., Editor 2, B., Eds.; Publisher: Publisher Location, Country, 2007; Volume 3, pp. 154–196, ISBN.
3. Author 1, A.; Author 2, B. *Book Title*, 3rd ed.; Publisher: Publisher Location, Country, 2008; pp. 154–196, ISBN.
4. Author 1, A.B.; Author 2, C. Title of Unpublished Work. *Abbreviated Journal Name stage of publication* (under review; accepted; in press).
5. Author 1, A.B. (University, City, State, Country); Author 2, C. (Institute, City, State, Country). Personal communication, 2012.
6. Author 1, A.B.; Author 2, C.D.; Author 3, E.F. Title of Presentation. In Title of the Collected Work (if available), Proceedings of the Name of the Conference, Location of Conference, Country, Date of Conference; Editor 1, Editor 2, Eds. (if available); Publisher: City, Country, Year (if available); Abstract Number (optional), Pagination (optional).
7. Author 1, A.B. Title of Thesis. Level of Thesis, Degree-Granting University, Location of University, Date of Completion.
8. Title of Site. Available online: URL (accessed on Day Month Year)